Results in Engineering 24 (2024) 102839

Contents lists available at ScienceDirect

Results in Engineering

journal homepage: www.sciencedirect.com/journal/results-in-engineering

Compact ultra-wide band two element vivaldi non-uniform slot MIMO antenna for body-centric applications

Sahar Saleh [a,b,*], Tale Saeidi [a,c], Nick Timmons [a], Bader Alali [d,e], Faroq Razzaz [f,g], Ayman A. Althuwayb [e]

[a] WiSAR Lab, Atlantic Technological University (ATU), Co. Donegal, F92 YY97, Letterkenny, Ireland
[b] Department of Electronics and Communications Engineering, Faculty of Engineering, Aden University, Aden, 5243, Yemen
[c] Electrical and Electronics Engineering Department, Faculty of Engineering and Natural, Sciences, Istinye University, Istanbul, 34326, Turkey
[d] Center for Wireless Communications (CWI), Institute of Electronics, Communications and Information Technology, Queens University, Belfast, Northern Ireland Science Park, Queen's Road, Queen's Island, Belfast, BT3 9DT, Northern Ireland, UK
[e] Electrical Engineering Department, College of Engineering, Jouf University, Sakaka, Aljouf, 72388, Saudi Arabia
[f] Electrical Engineering Department, College of Engineering, Prince Sattam Bin Abdulaziz University, Al-Kharj, 16278, Saudi Arabia
[g] Faculty of Engineering and Information Technology, Taiz University, Taiz, 6803, Yemen

ARTICLE INFO

Keywords:
Ultra-wideband (UWB)
MIMO
Vivaldi tapered slot antenna (VTSA)
Microstrip to slot (M/S) transitions
And CST

ABSTRACT

This work presents a novel compact two-port Vivaldi Non-uniform Slot MIMO Antenna (VNSMA) to overcome the challenges of traditional ultra-wideband (UWB) antennas, such as large size, limited bandwidth (BW), high mutual coupling, and suboptimal performance in wearable devices. Designed based on Vivaldi non-uniform slot profile antenna (VNSPA) theory, this antenna offers superior performance metrics and significantly advances wearable antenna technology. The novelty of this work is investigating different positions for the two compact UWB Vivaldi nonuniform Antennas (VNSAs) to get better performance with smaller sizes, wider impedance matching BW, and lower mutual coupling (MC) where side by side at an angle of 180° is determined to be the best configuration. Detailed parametric studies were performed on this configuration for better performance, where the MC was further reduced by etching the ground plane with a vertical slot between the two antennas and L slots around the Microstrip to Slot (M/S) transition, respectively. Furthermore, BW and gain enhancements were obtained by etching exponential tapered and triangular slots at its two edges. Using the Finite Integration Technique (FIT), Computer Simulation Technology (CST) software is used for the simulations in this work. The VNSMA is tested on a CST Gustav human phantom and gives excellent results with low specific absorption rate (SAR) values at several UWB frequencies. The proposed VNSMA provides good, measured outcomes of $S_{11} < -11.08$ dB with wide BW of 12.5 GHz (2.33–14.83 GHz) covering high isolation of −23 dB (for most of frequency band), moderate-high gain of 5.89 dBi, radiation efficiency of 66–90 %, low Envelope Correlation Coefficient (ECC) of 0.002 and high diversity gain (DG) of 9.99 dBi, stable radiation patterns, and average group delay of 1.2 ns. This innovative design, which optimizes antenna positioning and incorporates ground plane modifications, achieves remarkable improvements in BW, which covers multiple bands, including WLAN (2.4–2.485 GHz), X-band (8–12 GHz), and part of Ku band (12–18 GHz). The findings demonstrate the antenna's potential for various high-resolution microwave imaging applications, particularly in medical diagnostics like breast and brain cancer detection, showcasing its impact in wearable technology and healthcare.

1. Introduction

A wireless body area network (WBAN) comprises wearable computing devices. It establishes a wireless connection between wearable electronics and other communicating devices worn or implanted directly into the body. WBANs are seen as an integral part of the Internet of Things (IoT), as they can communicate with the cloud via cellular networks. WBAN's critical applications include health monitoring, entertainment (sports), surveillance, and first responder monitoring and protection, all simply incorporated into customer clothing [1]. Owing to

* Corresponding author. WiSAR Lab, Atlantic Technological University (ATU), Co. Donegal, F92 FC93, Letterkenny, Ireland.
E-mail address: sahar.saleh@atu.ie (S. Saleh).

https://doi.org/10.1016/j.rineng.2024.102839
Received 7 July 2024; Received in revised form 23 August 2024; Accepted 2 September 2024

its potential to enhance communication connections that may degrade due to reflection from high dielectric lossy tissues of the body, ultra-wideband (UWB) technology with a high data rate, low cost, low power consumption, and compact size is recommended for WBANs [2–4].

Since the UWB system has deficient radiated power (less than −41.3 dBm/MHz), the potential for interference with coexisting wireless applications is reduced. Receiving numerous signals from different directions at different phases causes multipath fading, degrading signal quality [5]. This may be mitigated by enhancing the communication system diversity using multiple input multiple output (MIMO) antennas to improve its reliability and capacity by converting nonconductive multipath fading into wireless transmission [6–9]. UWB MIMO technology is employed in wireless mobile communication due to its high data rate, broad operating bandwidth (BW), reliability, and improved channel capacity. MIMO antennas should be designed with small size and low mutual coupling (MC) to be compatible with small mobile handsets and strengthen diversity, respectively [10–12].

Different antenna topologies are proposed for designing the UWB MIMO system using a metallic or dielectric resonator radiator. The choice between metallic antennas and dielectric resonator antennas depends on the application's specific requirements, including frequency range, BW, size constraints, and the desired radiation characteristics [13,14]. Dielectric resonator antennas (DRAs) offer advantages in terms of BW and efficiency, especially at higher frequencies, while metallic antennas are versatile and widely used across many applications [15,16]. In Ref. [17], a UWB two elements rectangular DRAs MIMO system is designed for UWB communication systems with wide impedance bandwidth (3.29–10.74 GHz), high isolation (>-15 dB), and WLAN band rejection (4.98–6.08 GHz). The wide BW with high isolation and band rejection is achieved using a stub connected to the ground and two L-shaped parasitic strips attached to the dielectric resonator, respectively. Authors in Refs. [15,16] designed a stair-shaped dual rectangular dielectric resonator and a circular dielectric resonator UWB MIMO antennas. These antennas achieved wide BWs of 1.6–12.2 GHz and 1.58–8.4 GHz, respectively, using coplanar waveguide (CPW) and K-shaped microstrip feed networks. Additionally, they attained high isolation levels of 25 dB and 15 dB by incorporating extended metallic diagonal stubs and semicircular stubs in the ground plane. In Ref. [16], circular parasitic patches are loaded on the DRA elements to improve the isolation and the gain. However, in Ref. [18], a compact raked-shaped UWB dielectric resonator (DR) MIMO antenna was designed, operating over a BW of 3.52–10.89 GHz and fed by a transformer-type microstrip. In Ref. [19], a compact UWB aperture-stepped DR MIMO antenna was proposed, covering 3.7–10.8 GHz BW to enhance communication performance. The stepped structure of the DRs improved isolation in the higher frequency band while including a quarter-wavelength square patch in the neutralization line, which enhanced isolation in the lower frequency band. Additionally, the antenna's gain was increased by 37.84 %, and pattern stability was improved by integrating dual artificial magnetic conductors (AMCs). The antenna achieved impedance matching and high isolation by incorporating an inverted T-shaped parasitic strip and a partial ground plane. Recently, a circularly polarized (CP), wide BW (6.8–89 GHz) dual rectangular DR MIMO antenna has been proposed in Ref. [14] for WBAN application. The high isolation and CP are obtained by arranging the two DRs diagonally and using a unique H-shape feeding strip technique.

Based on the metallic radiator, slot antennas are suitable for designing MIMO systems when directive radiation, broad BW, easy integration with other circuits, and excellent isolation (low MC) are required without a decoupling structure [5]. Many types of UWB slot MIMO antenna with different miniaturization and MC reduction techniques are proposed. These antennas include general slot [6,20–22], stepped slot [10,12,23–28], common slotted ground (protruded ground) [7,27,29–31], or tapered slot [5,32–36] antennas.

Compact UWB two-element stepped slot MIMO antennas placed back-to-back [8,10,26,28] are designed for portable device applications. The high isolation in Refs. [8,10,28], and [26] is obtained by etching cross, T, and inverted T-shaped slots in the ground between the stepped slots, respectively. The isolation in their lower frequency band is enhanced by connecting a metal line in the decoupling cross-shaped slot, etching a narrow slit near the end of the two feeding ports, and etching a rectangular vertical slot near the top of the ground plane, respectively. An ultra-compact UWB (3.2–12 GHz) four-element stepped-slot MIMO antenna fed with a stepped microstrip feed line is proposed in Ref. [23] for portable UWB applications. Due to the asymmetrical element placements and inherent directional radiation properties, the antenna achieves a high isolation of −22 dB without requiring a decoupling structure. The elements are arranged asymmetrically, with two elements parallel to the other two sets. The steeped feed line and slots, which ease the mode resonance transition, produce improved matching and BW.

In [25], surrogate-based optimization (SBO) is used to optimize the UWB two-element stepped slot MIMO antenna dimension for compactness and low MC. The compactness is accomplished by utilizing a triangular layout for each antenna rather than a rectangular one. However, the isolation is enhanced and controlled by placing the elements orthogonally and adjusting the distance between them using a simple 45° oriented slot. The same concept is employed in the design of the UWB (2.94–14 GHz) four ports half-cutting circular slot MIMO antenna [20], which achieves 50 % compactness by cutting the circular patch in half using an asymmetric feeding scheme (AFS). The antenna's better matching and isolation were achieved by employing ten metal-filled vias in the feed line and aligning the elements orthogonally. Also, 50 % compactness is achieved in the proposed compact UWB (2–10.93 GHz) 2 elements MIMO antenna for portable UWB communication systems [6] by cutting the circular patch and ground by half. In this design, a new fence-type decoupling structure with multiple slits and three segments of microstrip lines (which function as bandstop filters) is employed to improve isolation between the two ports at high frequencies. However, the isolation at low frequency (3–3.4 GHz) is enhanced using L-shaped parasitic branches.

Dual polarization or diversity in the MIMO system can be obtained by placing the antennas orthogonally, which is required to mitigate the multipath fading effect. Orthogonal configuration is used to increase the high isolation of the proposed dual-band (WLAN (2.4–2.485 GHz and 3.1–12.5 GHz) two-port pentagonal wide slot [21] and UWB (2.3 – >12 GHz) two-port L-shaped slot [31] MIMO antennas proposed for MIMO diversity applications. They are fed by U- and square-shaped patches for BW improvement, respectively. A narrow quarter wavelength rectangular slot is etched on the ground plane of the MIMO antenna in Ref. [31] to reduce the mutual coupling at the lower frequency band (3–4.5 GHz). The CPW fed dual-polarized UWB (2.5–12.5 GHz) two-port annular slot [7], wideband (Bluetooth, WLAN, WiMAX, and UWB) two-port circular ring slot [29], UWB (2.8–11 GHz) two-port circular ring slot [7], and UWB (3.1–12 GHz) two-port rectangular slot [27] MIMO antennas with high isolation are proposed for portable MIMO/diversity applications. In addition to the orthogonal configuration, their high isolations are obtained by introducing a cross-, fork-, rectangular-, and Minkowski fractal-shaped stub diagonally at 45°, between the CPW fed ports, respectively. Additionally, the U-shaped stub [7] and staircase-shaped [27,29,30] stubs of the CPW-fed ports are used for impedance matching and BW enhancements.

The first UWB (3.13 – >11 GHz) two closely packed (placed back-to-back) linear tapered slot MIMO antenna in Ref. [5] with high isolation of < −22.55 dB was proposed for short range and high data rate UWB wireless communication. The high isolation is obtained due to its directional properties and etching quarter wave slot resonator, which prevents the current from flowing from one port to another. The current will accumulate on the short end of the quarter wave slot and will be weak when it reaches the open end in the center, preventing it from being distributed to the port of the second antenna. The same arrangement of placing the antennas back-to-back proposed in Ref. [5] is used to

design UWB MIMO Vivaldi tapered slot antennas for UWB wireless communication applications using two-element antennas in (2.7–10.9 GHz) [32], (2.9–11.6 GHz) [33], and (2.5–12 GHz) [34] and a four-element in (3–12.3 GHz) [36] with more compactness due to the reduced ground size. The high isolation and compactness in Refs. [32, 33] are obtained by etching a T-shaped slot between the feeds. In Ref. [34], they are obtained by etching a T-shaped slot between the feeds and loading four absorption resistors on the ground, respectively. The MC between the ports in Ref. [36] is reduced by etching slots and fence-type structures at the ground plane and loading I-shape branches between the radiating ports. Low and high-frequency BWs are enhanced by loading resistor and rectangular patch at the opening of the conical gap and in the middle of the conical groove, respectively. Also, the patches are used to optimize the radiation pattern at high frequencies.

The literature shows that the UWB stepped slot and common slotted ground (protruded ground) MIMO antennas are preferred for mobile communication due to their small size, wide BW, reduced MC, and omnidirectional radiations. The wide BW and small size are attributed to the increased resonance frequency and electrical length, respectively [23]. However, UWB tapered slot MIMO antennas with their simple planner structure, low profile, lightweight, low fabrication cost, and easy integration with circuits, wide BW, high gain, and directive radiation patterns (end fire (E-plane) and omnidirectional (H-plane)) are preferred for high resolution and precise detection applications such as microwave imaging (MWI) detection. Also, they can be used for WBAN applications to enhance the communication link that may degrade due to the high dielectric losses of human tissues.

Table 1 outlines the pros and cons of these related two elements UWB MIMO slot antennas in terms of gain, MC, size, diversity performance (Envelope Correlation Coefficient (ECC) and high diversity gain (DG)), group delay (GD), on-body and specific absorption rate (SAR) calculations (to assess its suitability for WBAN applications). V, GS, SS, and SPG in Table 1 are referred to as Vivaldi, general slot, stepped slot, and slot with protruded ground antennas, respectively. More details regarding their performance regarding the measured results and enhancement techniques will be explained at the end of Section 3.

In this work, based on Rogers RO4003C substrate ($\varepsilon_r = 3.55$, $\tan\sigma = 0.0027$ and 0.813-mm thickness), compact UWB two elements Vivaldi MIMO antenna (VNSMA) is designed based on Vivaldi non-uniform slot profile antenna (VNSPA) theory [37]. The novel UWB VNSA with 51.94 % size reduction, 2.91 % improved BW, and 5.8 % improved peak gain, is exploited to get compact UWB VNSMA with enhanced performance of wide BW, high isolation, ECC, DG, stable gain, and directive radiation patterns.

The objectives of this work can be summarized as follows.

1. **Optimize Antenna Placement**: Investigate various placements of the two VNSAs to optimize performance, focusing on compactness, high isolation, broad impedance matching, and high gain.
2. **Conduct Parametric Studies**: Perform detailed parametric studies on the selected MIMO configuration to achieve further improvements
3. **Evaluate Performance in Wearable Applications**: Test the proposed MIMO antenna on a CST Gustav human phantom and calculate the SAR values to ensure its suitability for wearable applications.

The advantageous features of the proposed UWB VNSMA make it a good candidate for general wearable applications, particularly those requiring higher resolution and precise detection, such as breast [3] and brain [38] cancer detection. The novelty of this work can be summarized as follows.

- Exploit the sound characteristics of the compact UWB VNSA to design a compact UWB MIMO antenna
- Investigating various placements of the two VNSAs for better performance in terms of compactness, high isolation (−23 dB), broad impedance matching (12.5 GHz), high gain (5.89 dBi), low ECC (0.002) and high DG (9.99dBi)
- Detailed parametric studies are performed on the selected MIMO configuration to help improve performance, which results in a 3.72 % size reduction and 17.41 % BW improvement compared to a single VNSA. The resulting BW (2.66–15.1) covers WLAN, X-band, and part of the Ku band

In addition to this section, Section 2 discusses the antenna design and analysis using Computer Simulation Technology (CST) software, and Section 3 demonstrates the results and discussions. Finally, Section 4 outlines the research conclusions.

Table 1
The pros and cons of the state-of-the-art two elements UWB slot MIMO antennas.

Ref., Type	Dimensions mm × mm × mm	Pros.	Cons.
[5], V	60 × 40 × 0.8	• Low MC	• low gain • large size • not super wide BW (7.87 GHz) • diversity performance (DG only simulation) • on body and SAR calculations are not included • GD is not included
[21], GS	56 × 28 × 1	• Low MC	• low gain • large size • not super wide BW (9.4 GHz) • diversity performance (ECC: only simulation, DG: NA) • on body and SAR calculations are not included • GD is not included
[29], SPG	48 × 48 × 0.8	• low MC • high gain • wide BW (10.2 GHz)	• large size • diversity performance (DG: NA) • on body and SAR calculations are not included • GD is not included
[31], SPG	32 × 32 × 0.8	• low MC • small size	• low gain, • not super wide BW (9.7 GHz) • diversity performance (DG only simulation) • on body and SAR calculations are not included • GD is not included
[28], SS	22 × 36 × 0.8	• low MC • small size	• low gain, • not super wide BW (8 GHz) • diversity performance (DG: NA) • on body and SAR calculations are not included • GD is not included
[8], SS	22 × 26 × 1.524	• small size • high gain	• high MC • not super wide BW (7.87 GHz) • diversity performance (DG: NA) • GD is not included
[25], SS	21 × 30 × 0.762	• low MC • small size	• not super wide BW (8.6 GHz) • low gain • diversity performance (NA) • on body and SAR calculations are not included • GD is not included
[6], GS	50 × 35 × 1	• low MC	• not super wide BW (8.93 GHz) • large size • diversity performance (ECC: only simulation, DG: NA) • on body and SAR calculations are not included • GD is not included

NA: not available.

2. Methods

This section focuses on the design and analysis of the proposed VNSMA. Subsection 2.1 discusses the selection and arrangement of MIMO elements. Subsection 2.2 presents detailed parametric studies on the chosen arrangement to enhance compactness and performance. Finally, Subsection 2.3 explores the VNSMA's impact on the human body using a CST-based voxel model and calculates the specific absorption rate (SAR) to ensure the prototype antennas are efficient for UWB wearable applications with low SAR.

2.1. Design evolution

A novel UWB Vivaldi Non-uniform Slot Antenna (VNSA) with 51.94 % size reduction, 2.91 % and 5.8 % improved BW and peak gain (PG), respectively, were obtained by further reducing the size of the compact UWB Vivaldi Tapered Slot Antenna (VTSA) proposed in Ref. [39] using VNSPA theory developed in Ref. [37]. Details on how the theory is developed and applied to the Vivaldi antenna can be found in Refs. [37,40]. The design simplicity of the single antenna is a crucial advantage where VNSPA theory offers a straightforward approach to achieving the desired compactness while maintaining high performance for the Vivaldi Tapered Slot Antenna (VTSA). This method avoids the complexities and high costs associated with previous techniques, such as adding resistive and dielectric loads, corrugations, and grating elements for gain and bandwidth enhancement. The novelty of this work is to exploit the compact UWB VNSA to design a compact UWB two-element VNSMA with high isolation, gain, and enhanced BW by investigating various placements of the two elements and modifying the design for better performance. Determining the optimal arrangement of the VNSMA elements is straightforward through simulation, focusing on matching, isolation, and size. Furthermore, additional compactness and performance improvements were achieved through design modifications and parameter sweeps, as detailed in this section and Subsection 2.2, respectively, without additional matching or decoupling structures.

According to the literature, to achieve high isolation with slot antennas, it is preferable to place them orthogonally or opposite each other (back-to-back), with some decoupling structure (most commonly: slots and narrow slits) between them to prevent the current flow from one port to another through the shared ground plane. The coupling usually happens between the two elements due to the ground surface current and near field [8]. Based on [21], different configurations for placing the two elements are explored here to improve the VNSMA compactness, diversity, and matching. As illustrated in Fig. 1(a–c), the two antennas are placed face-to-face (F2F), face-to-back (F2B), and back-to-back (B2B), respectively. It should be noted that the feeds in F2F, F2B, and B2B are oriented in opposing directions to avoid overlapping. As illustrated in Fig. 1(d–f), in addition to these configurations, the antennas are placed side by side (SBS) with 0° (SBS0°), 90° (SBS90°), and 180° (SBS180° or parallel as in Ref. [21]). The SBS90° configuration is the same as in Ref. [41]. The size and simulated S-parameters results of these six configurations are shown in Table 1. Although orthogonal feeding is typically used to get more compactness and high isolation [7,21,29,31], the compactness in Refs. [7,29,31] is obtained due to the shared ground slot. However, as depicted in Table 2 and Fig. 1(e), the arrangement of antennas in SBS90° increases the size due to the difficulty of using one common ground slot for the two VNSAs compared to the antennas with common slot ground and stub radiators [7,21,29,31].

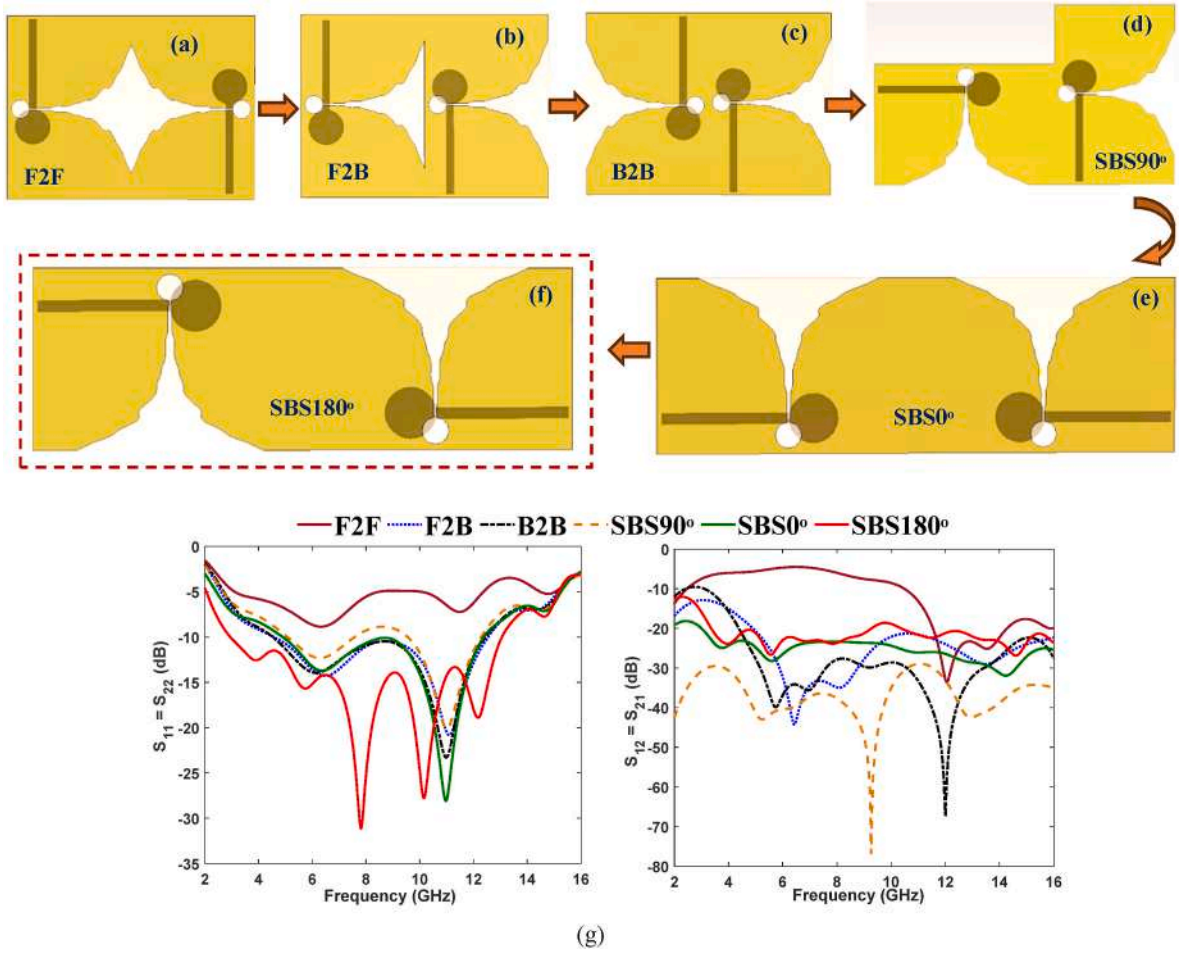

Fig. 1. Different MIMO configurations based on UWB VNSA (a) F2F, (b) F2B, (c) B2B,(d) SBS0° (e) SBS90°, (f) SBS180° and (g) simulated S-parameters.

Table 2
Size and simulated S-parameters of the different VNSMA configurations.

Antennas	F2F	F2B	B2B	SBS0°	SBS90°	SBS180°
Size (mm^2)	1199.392	1199.392	1199.392	1199.392	1490.656	**1199.392**
S_{11}(dB)<	Not matched	−10.38, 4.51–12.43, 7.92	−10.44, 4.57–12.54 ,7.97	−10.08, 4.9–12.38, 7.48	−8.82, 5.09–12.26, 7.17	**−11.52, 2.95–13.06, 10.11**
S_{12}(dB)<	−4.5	−22.16	−19.9	−23.27	−28.9	**−20.34, -15.37, 2.95–4.75 −18.59, 9.25–10.25**

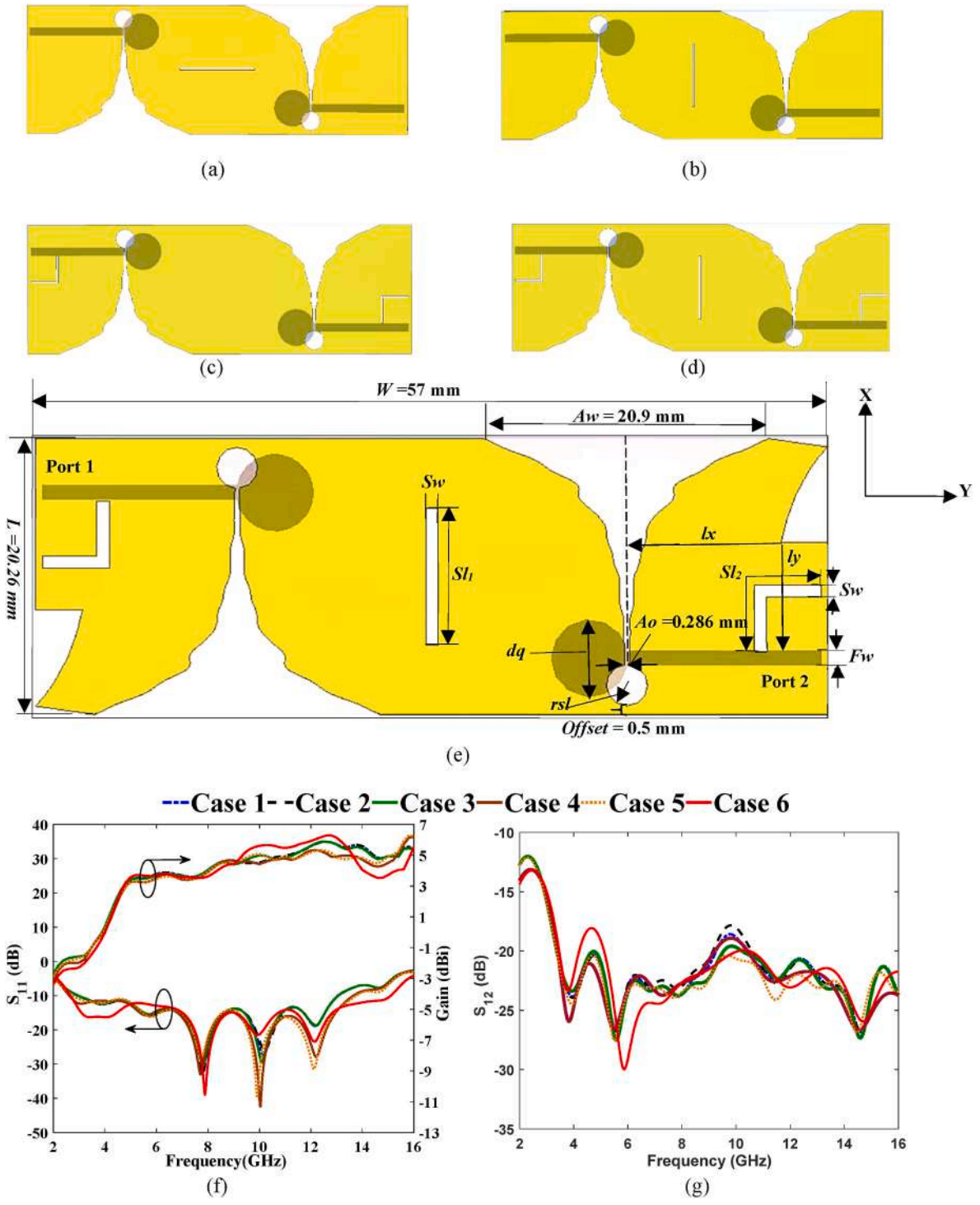

Fig. 2. Modification of the proposed UWB VNSMA SBS180° (Case 1) towards performance enhancement (a) Case 2, (b) Case 3, (c) Case 4, (d) Case 5 (e) Case 6, and (f) simulated S_{11} with gain, and (g) simulated S_{12}.

Furthermore, the impedance matching is worse than others, although providing the best reduced MC. Also, it can be seen that for F2B, B2B, and SBS0°, the BW is reduced, and the matching is degraded despite the reduced MC within the band. In Refs. [6,20,25], the compactness for symmetrical and asymmetrical (using the AFS technique) slot MIMO antennas with SBS180° configuration is achieved by cutting the antenna in half or removing a triangular space, respectively. Based on AFS, the feeding should be modified to avoid the mismatching caused by high input impedance due to the cutting. However, this can not be done for VNSA due to asymmetry in the feed line, where a quarter wavelength stub is needed in the M/S transition for matching. As shown in Fig. 1(g) and Table 2, SBS180° is selected due to its better matching, wider BW, and reasonably reduced MC.

According to the analysis above, SBS180° is selected due to its better matching, wider BW, and acceptable isolation of < -20 dB. Due to the significant role of Defected Ground Structure (DGS) techniques in enhancing antenna performance by modifying the current distribution on the ground plane, which impacts parameters such as impedance matching, MC, BW, and radiation pattern, two types of DGS are employed [4,9,42,43]. A vertical slot is placed at the center between the antennas, while L-shaped slots are placed around the M/S transition of each antenna. Etching a T-shape slot in the ground between the feedlines of the antennas will enhance the isolation and impedance matching BW while etching a quarter wavelength narrow slit will improve the isolation at the lower frequency band [5,8,10,31]. The T-slot will alter the current distribution and extend its path, decreasing the first resonant frequency and increasing the matching BW. On the other hand, the slot will increase the distance between the feed lines and suppress the surface currents, enhancing the isolation. In the narrow slit, the current tends to gather at the shorter end of the quarter-wave slot, resulting in its weakening by the time it reaches the open end at the center. This hinders its effective distribution to the port of the second antenna [5]. The T-shape slot is suitable for a slot MIMO antenna when its elements are orthogonally or opposite. In this case, the slot is etched between the feed lines to increase the distance between them and improve isolation. However, a T-shape slot is not used in this work because the two feed lines are already placed far away. For this reason, only the narrow slit is added to the selected VNSMA SBS180°.

For comparison with other cases where slots are added, Case 1 will be referred to the selected VNSMA SBS180°, where no slots are added. As illustrated in Fig. 2(a) and (b), narrow horizontal (Case 2) and vertical slots (Case 3), respectively, are etched between the two elements of Case 1 (shown in Fig. 1(f)). As shown in Fig. 2(g), using a vertical slot in Case 3 provides better isolation than the horizontal one in Case 2. Case 4 is then obtained by adding the L slots around the feed line of Case 1, as illustrated in Fig. 2(c), and this will excite more resonances and widen the BW compared to previous cases (Case 1, 2, and 3). Since wider BW and better isolation are obtained for Case 3 and Case 4, as illustrated in Fig. 2(f) and (g), respectively, as compared to Case 1 and 2, both vertical and L slots are added in Case 5 (Fig. 2(d)). As illustrated in Table 3 and Fig. 2(g), for Case 5, better isolation (<-20.36 dB) is obtained at all the bands except at the lower narrow band; this is reduced to $<$ -13.94 dB which is acceptable. The main issue with Case 5 is the low PG (5.36 dBi) achieved due to the L slots of Case 4 (5.32 dBi), which is the lowest compared to the others (Case 1 (5.89 dBi), Case 2 (5.88 dBi), and Case 3 (5.8 dBi)), as shown in Fig. 2(f). It is due to the amount of current accumulated in the L-slot, which decreases the current delivered to the transmission feed line.

To solve the low gain problem, exponentially tapered slots (Ae^{tx}) are added to the VNSMA edges and triangular slots are added at its edge top corner connecting the tapered slot to the aperture width, *Aw* (Case 6) as shown in Fig. 2(e). *t* is the tapering rate; *A* is equal to the half of aperture opening (A_t) of this tapered slot and *x* is the distance along the tapered slot length (L_t). The effect of using the slots in enhancing the BW and matching can be noticed in the current distribution around the edges of the slot for Case 6 in Fig. 3 compared to Case 1. As illustrated in Fig. 2(f) and (g), and Table 3, although the isolation in Case 5 is higher than in Case 6, it is selected due to its 1.16 GHz wider BW, 0.57 dB better matching, and 0.91 dBi higher PG and the obtained isolation is still acceptable for UWB application. It should be noted that the slot lengths for Case 2, Case 3, and Case 4 are 11.84 mm, 10 mm, and 8.6 mm, respectively, which are better than the calculated ones at 3.1 GHz ($\lambda/4 = 12.8$ mm), and the optimum slot width is 0.3 mm. The layout of the selected case (Case 6) is shown in Fig. 2(e) where *Ao*, *W*, *L*, Sl_1, Sl_2, *Fw*, *Sw*, *dq*, *rsl, ds*, *offset*, *lx,* and *ly* are the aperture opening, VNSMA width, VNSMA length, length of the vertical slot, length of the L slot, feed line width, slot width, diameter (quarter wavelength) of microstrip stub in the M/S transition, the radius of the slot in the M/S transition antenna (*dq*/2), the width of one element without *dq*, the remaining distance of the non-slotted copper in the x-axis, the distance from half antenna width (one element), and the distance from *Fw*, respectively. A detailed parametric study for the proposed UWB VNSMA (Case 6) is discussed in the next section.

The impact of adding vertical and L slots on reducing the MC (between the two antennas of the proposed VNSMA can be seen in the surface current distributions of Case 1 and Case 6 in Fig. 3 at different frequencies within the UWB. Case 1's current is distributed equally at both ports, where more current follows in the ground from one antenna to another [6], and the possibility of coupling is greater. The current distribution in Case 6 is different, which is more at port 1 (P1) when excited, indicating reduced coupling with port 2 (P2) owing to the usage of vertical and L slots. The low isolation at the lower frequency band for Case 6 can be explained by the equal current distribution between its ports, as depicted in Fig. 3(b). This effect is further illustrated by the electric field distribution for Case 1 (without slots) and Case 6, as shown in Fig. 4, when port 1 is excited. The distribution reveals a weak electric field around the slot, particularly at 4 and 8 GHz frequencies, as illustrated in Fig. 4(a) and (b), respectively. Both cases exhibit low MC at higher frequencies, as shown in Fig. 4(c).

2.2. Parametric studies on antenna structure

In addition to assessing the surface current and electric field distributions as performance indicators, particularly regarding mutual coupling (MC), this section evaluates the convergence behavior of the optimization process through the parameter sweep in CST. This evaluation involves monitoring the stabilization of key performance metrics, such as impedance matching within the required UWB bandwidth while maintaining moderate high gain, analyzing the rate of change between iterations, and reviewing the optimization history for consistency.

Table 3
Simulated S-parameters of different cases of the UWB VNSMA (SBS180°).

Antennas	Case 1	Case 2	Case 3	Case 4	Case 5	Case 6
S_{11}(dB)<, PG(dBi)	−11.52, 2.95–13.06, 10.11, 5.89	−11.52, 2.95–13.06, 10.11, 5.88	−11.93, 2.96–13.07, 10.74, 5.8	−11.5, 2.6–13.65, 11.05, 5.32	−10.95, 2.76–13.75, 10.99, 5.36	**−11.52, 2.95–15.1, 12.44, 6.27**
S_{12}(dB)<	−20.34, −15.37 (2.95–4.75),-18.59 (9.25–10.25)	−20.36, −15.44 (2.95–4.75),-17.85 (9.25–10.25)	−19.59, 15.33 (2.96–4.63)	−21.06, −13.4 (2.6–3.49),-18.92 (8.92–10.72)	−20.6, −13.9 (2.76–3.42)	**−19.94, -13.34 (2.66–3.32),-18.06 (4.21–5.1)**

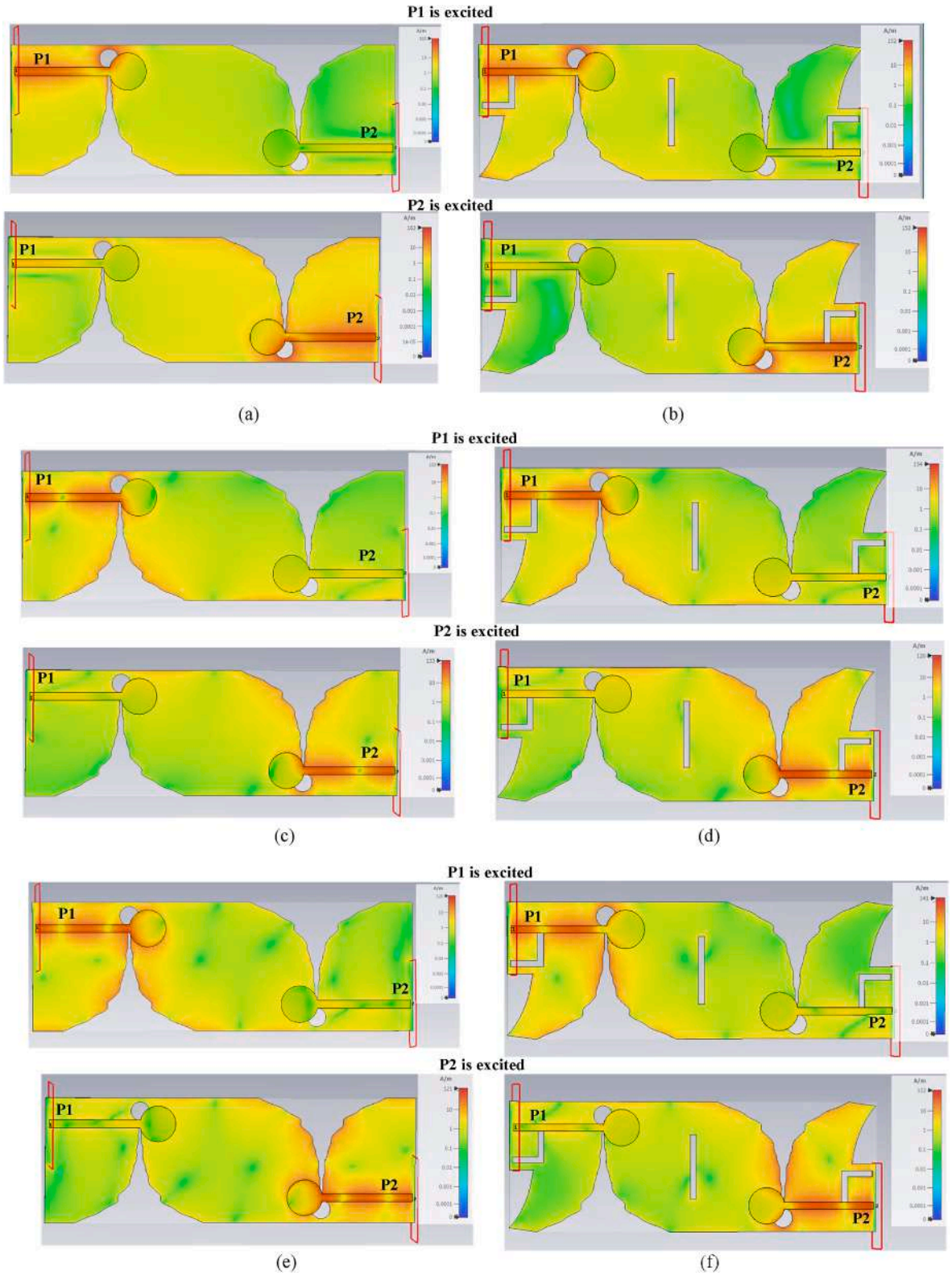

Fig. 3. Simulated surface current distribution for Case 1 (left) and Case 6 (right) at (a), (b) 4 GHz, (c), (d) 8 GHz, and (e), (f) 12 GHz.

Convergence was confirmed when performance metrics stabilized, with results showing $S_{11} < -12.15$ dB at 2.66–15.1 GHz, PG of 6.27 dBi, and $S_{12} < -19.94$ dB over most of the band, including −13.34 dB at 2.66–3.32 GHz and −18.06 dB at 4.21–5.1 GHz.

The BW and matching of the Vivaldi antenna are mainly affected by the M/S transition parameters (*dq* and *rsl*) by which the power is transmitted from the circular stub to the circular slot via electromagnetic coupling. As shown in Fig. 5(a) and Table 4, BW and gain improve as *dq* decreases; however, the matching degrades, and *dq* of 5.7 mm is selected due to its better matching and isolation compared to other values (*dq* = 5.4 mm, 5.5 mm and 5.6 mm). Etching a slot in the antenna ground plane will excite more resonances and enhance the matching and

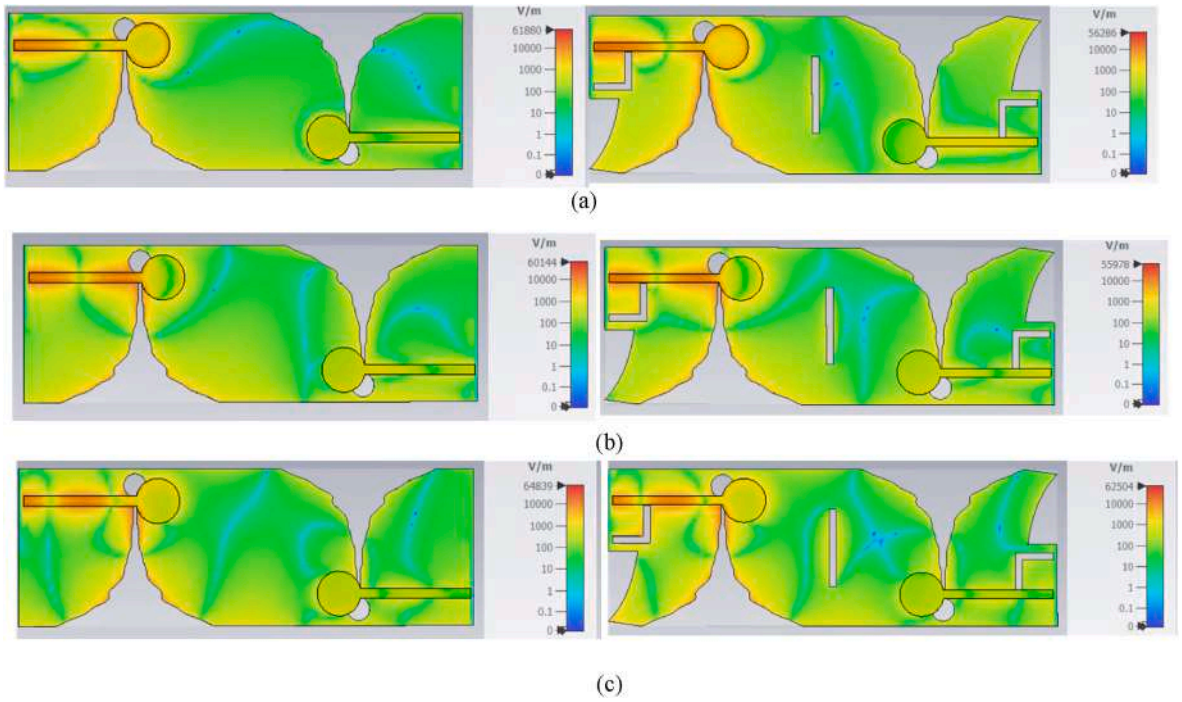

Fig. 4. Simulated electric field distribution for Case 1 (left) and Case 6 (right) at (a) 4 GHz, (b) 8 GHz, and (c) 12 GHz.

BW, and this can be seen in Fig. 5(b) and Table 4; when *rsl* increases, the matching and BW improve. *rsl* = 1.505 mm is selected due to its better matching and BW, although of 0.47 %, 0.16 %, and 0.95 % PG enhancement at *rsl* = 1.203 mm, 1.305 mm, and 1.405 mm, respectively. The effect of *dq* and *rsl* on the antenna matching, BW, and gain can be explained by the amount of power coupled from the stub to the slot. As the *rsl* is less than (*dq*/2 = 2.85 mm), gain and BW will increase if *dq* is reduced to fit this small *rsl,* and this can be noticed in Fig. 5(a) and Table 4, where the gain increases as *dq* decreases. Matching is enhanced by selecting the suitable *dq* and *rsl* to couple the signal correctly. Another critical parameter affecting matching is *Fw*, and as shown in Fig. 5(c) and Table 4, with *Fw* = 1.1 mm, the antenna achieves the best matching, which is better than the calculated one at the design frequency (for 50 Ω, *Fw* = 1.82 mm). With *dq* = 5.7 mm, the effect of *ds* on the VNSMA performance is studied. As shown in Fig. 5(d) and Table 4, *ds* = 22.8 mm is chosen because it outperforms *ds* = 19.8 mm and 21.8 mm in terms of matching, BW, gain, and isolation and outperforms 20.8 mm in terms of BW, gain, and isolation.

Changing the parameters of the exponentially tapered slot, L_t, *t,* and A_t have no significant effect on the antenna performance, and the selected values are 19 mm, 0.21, and 0.3 mm, respectively, as shown in Fig. 4(e) for L_t (*t* and A_t have the same results as L_t). Although etching tapered and triangular slots improves antenna BW by triggering additional resonance, we must be careful about matching and gain. *Aw* decreases because the triangular slot area increases as the slot approaches the aperture main slot. Hence, the gain decreases, as seen in Fig. 5(f) and Table 4, where the antenna gain decreases as *lx* increases. *lx* = 10.3 mm is selected due to its better matching and wider BW than *lx* = 9.3 mm, 11.23 mm, and 12.3 mm and higher gain than *lx* = 11.3 mm and 12.3 mm. Moving the tapered slots toward *Fw* (*ly*) does not affect antenna performance, as illustrated in Fig. 5(g). The vertical slot is added to enhance the isolation between the two elements. As illustrated in Fig. 5 (h) and Table 4, as Sl_1 decreases, the isolation is improved; however, Sl_1 = 10 mm is selected due to its better matching than other values (Sl_1 = 9 mm, 11 mm, and 12 mm). Although the isolation at the lower frequency bands is enhanced at Sl_2< 9.8 mm for the L slot, as shown in Fig. 5(i) and Table 4, Sl_2 = 9.8 mm is selected due to its higher gain than Sl_2 = 5.8 mm and 7.8 mm. It also provides better matching and wider BW than Sl_2 = 5.8 mm and 11.8 mm. As shown in Fig. 5(j), the slot width (*Sw*) has no significant effect on the isolation; however, the gain increases as *Sw* increases, and *Sw* = 0.9 mm is selected due to its better matching. As compared to the compact size of UWB VNSA (29.6 mm × 20.26 mm × 0.813 mm) [37], the size of the single element (28.5 mm × 20.26 mm × 0.813 mm) in the proposed VNSMA is reduced by 3.72 %, and the BW is enhanced by 17.41 %. Based on these optimized parameters, Sl_1 = 10 mm, Sl_2 = 9.8 mm, *Fw* = 1.1 mm, *Sw* = 0.9 mm, *dq* = 5.7 mm, *ds* = 22.8 mm, *rsl* = 1.505 mm, *t* =0.21, A_t = 0.3 mm, L_t =19 mm *lx* = 10.3 mm and *ly* = 6 mm, the UWB VNSMA is fabricated as illustrated in Fig. 6. It's important to note that the negative gain in the lower frequency band is due to MC between the two elements, as well as the reduced size. The MC and compactness lead to destructive interference and phase cancellation across the antenna [41], ultimately leading to low or negative gain in the lower frequency band. Future work will improve isolation between the elements to achieve a higher gain in these lower-frequency bands. Measured results are discussed in the next Section.

2.3. On body effect and SAR calculation

In this section, we will explore the influence of the human body on antenna performance as well as calculate the specific absorption rate (SAR) to ensure the efficiency of prototype antennas for UWB wearable applications with low SAR.

As illustrated in Fig. 7(a), the proposed UWB VNSMA is placed on the shoulder of the CST voxel model (Gustav) at different distances (0 mm, 5 mm, 10 mm) to test its efficiency for wearable applications in the presence of high dielectric body tissues. As shown in Fig. 7(b), (c), and 7 (d), when the antenna is placed close to the body (a frequency-dispersive medium), it induces a current that can act as a receiving antenna, potentially establishing human body communication (HBC). This interaction can negatively impact the performance of the wearable device [44,45]. The high conductivity and absorption of human body tissues resulted in broader impedance matching, low gain, and high MC between the ports in case of close distances (0 mm and 5 mm). To mitigate this, the distance between the antenna and the body should be increased to create an air gap for isolation [1]. 10 mm is found to be

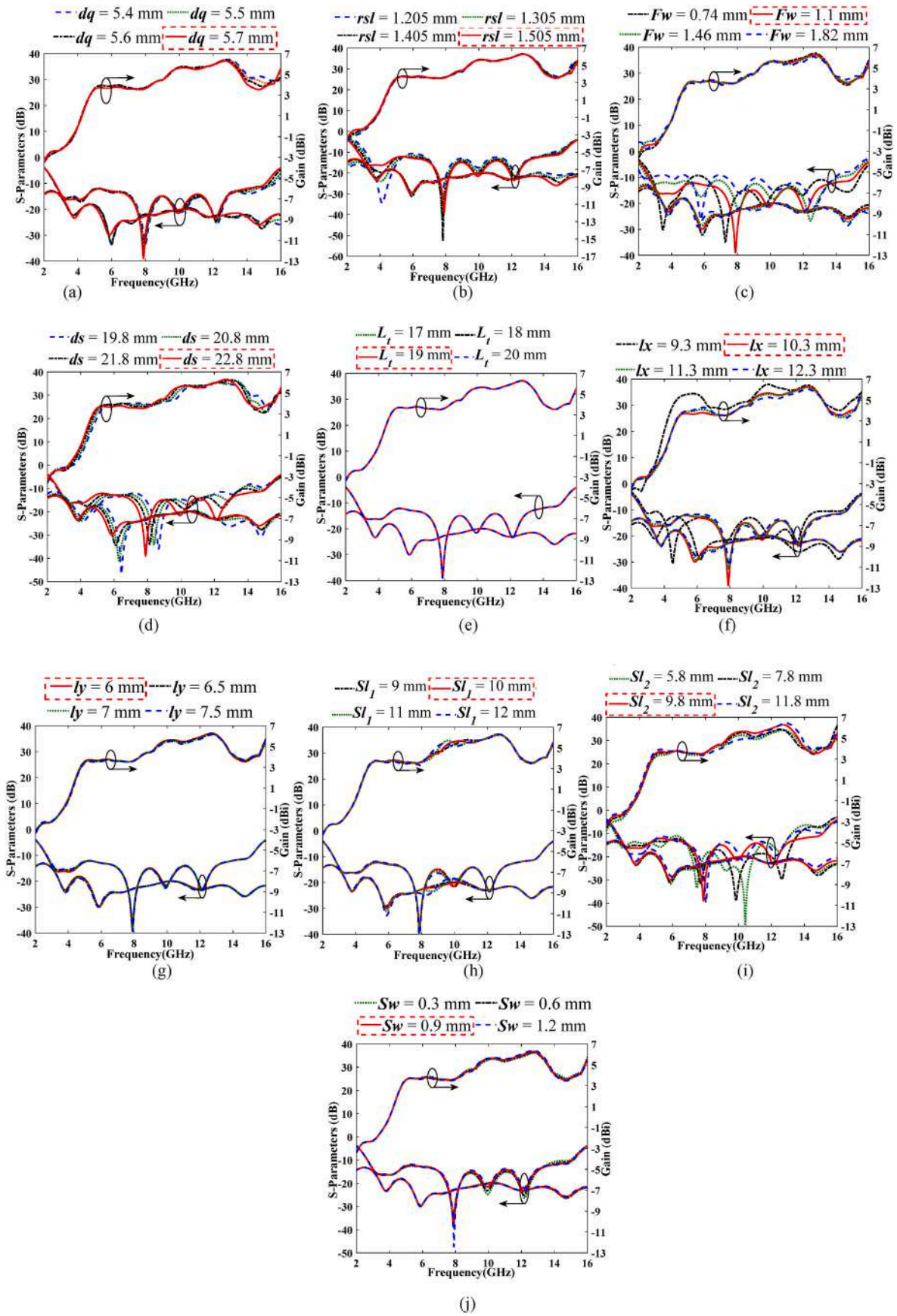

Fig. 5. Parametric study of the proposed UWB VNSMA on (a) *dq*, (b)*rsl*, (c) *Fw*, (d) *ds*, (e) A_t, (f) *lx*, (g) *ly*, (h) Sl_1, (i) Sl_2 and (j) *Sw*.

Table 4
Parametric study of the proposed VNSMA.

Par.	Parameter value (<-S_{11}(dB), Frequency Band (GHz), PG (dBi))			
dq	5.4 (11.78, 2.61–15.66, 6.42)	5.5 (11.92, 2.63–15.5, 6.41)	5.6 (12.09, 2.64–15.31, 6.36)	**5.7 (12.15, 2.66–15.1, 6.27)**
rsl	1.205 (10.62, 3.13–14.5, 6.3)	1.305 (10.61, 3.12–14.51, 6.28)	1.405 (10.85, 2.83–15, 6.33)	**1.505 (12.15, 2.66–15.1, 6.27)**
Fw	0.74 (9.3, 2.79–15.41, 6.34)	**1.1(12.15, 2.66–15.1, 6.27)**	1.46(11.1, 2.54–14.17, 6.1)	1.82 (9.01, 2.3–13.95, 6.1)
ds	19.8 (11.5, 2.6–13.68, 6.03)	20.8 (12.57, 2.65–13.62, 6.13)	21.8 (10.07, 2.65–15.14, 6.21)	**22.8(12.15, 2.66–15.1, 6.27)**
lx	9.3 (10.49, 2.78–14.91, 6.48)	**10.3 (12.15, 2.66–15.1, 6.27)**	11.3 (11.58, 2.68–15.11, 6.19)	12.3(11.46, 2.71–15.13, 6.02)
Sl_1	9 (11.72, 2.66–15.11, 6.31)	**10 (12.15, 2.66–15.1, 6.27)**	11 (11.48, 2.66–15.03, 6.24)	12 (11.51, 2.66–15.10, 6.3)
Sl_2	5.8 (11.12, 2.53–13.22, 5.77)	7.8 (12.3, 2.62–13.67, 5.84)	**9.8 (12.15, 2.66–15.1, 6.27)**	11.8 (11.36, 2.67–13.33, 6.37)
Sw	0.3 (10.31, 2.67–14.94, 6.14)	0.6 (11.13, 2.67–15.05, 6.19)	**0.9 (12.15, 2.66–15.1, 6.27)**	1.2 (11.61, 2.68–15.12, 6.44)
	Parameter value (<-S_{12}(dB), Frequency Band (GHz), PG (dBi))			
dq	5.4(19.44, 18.07(4.29–5.23),13.03 (2.61–3.3)	5.5(19.46, 13.14(2.63–3.27),18.06 (4.27–5.23)	5.6(19.57, 13.25(2.64–3.26),18.1 (4.23–5.22)	**5.7(19.94, 13.34(2.66–3.32),18.06 (4.21–5.1)**
rsl	1.205(19.69, 18.44(4.24–5.06),17.63 (3.13–3.23)	1.305(19.75, 16.87(3.12–3.29),18.4 (4.22–5.08)	1.405(19.94, 14.56(2.83–3.29),18.5 (4.19–5.13)	**1.505(19.94, 13.34(2.66–3.32),18.06 (4.21–5.1)**
Fw	0.74(19.95, 18.22(4.18–5.09),14.63 (2.79–3.31)	**1.1(19.94, 13.34(2.66–3.32),18.06 (4.21–5.1)**	1.46(20,18.37(4.27–5.1),12.75 (2.54–3.35))	1.82(20.04, 18.06(4.35–5.12),10.2 (2.31–3.29)
Ds	19.8(19.58, 11.48(2.6–3.46), 16.93 (4.64–5.68))	20.8(19.76, 14(2.68–3.36), 17.45 (4.28–5.32))	21.8(19.61,12.34 (2.64–3.46),17.46 (4.43–5.45))	**22.3(19.94, 13.34(2.66–3.32),18.06 (4.21–5.1)**
Lx	9.3(20.4, 13.43(4.06–5.3), 16.06(2.78))	**10.3(19.94, 13.34(2.66–3.32),18.06 (4.21–5.1)**	11.3(19.83,13.66(2.68–3.28),17.68 (4.2–5.2))	12.3(19.68, 13.79(2.71–3.25),17.76 (4.23–5.18)
Sl_1	9(19.94, 13.43(2.66–3.33), 18.22 (4.23–5.1))	**10(19.94, 13.34(2.66–3.32),18.06 (4.21–5.1)**	11(18.92,13.45(2.66–3.32),17.95 (4.33–4.99))	12(18.42, 13.4(2.66–3.3),17.72 (4.37–4.94)
Sl_2	5.8(20.04, 13.8(2.53–3.36), 18.8 (4.3–5.05))	7.8(19.78, 13.5(2.62–3.36),18.51 (4.29–5.03)	**9.8(19.94, 13.34(2.66–3.32),18.06 (4.21–5.1)**	11.8(20.39, 13.4(2.68–3.24),16.83 (4–5.32)
Sw	0.3(19.74, 13.45(2.67–3.37), 18.27 (4.27–5.07))	0.6(19.84, 13.5(2.67–3.34), 18.17 (4.24–5.09))	**0.9(19.94, 13.34(2.66–3.32),18.06 (4.21–5.1)**	1.2(20.04, 13.44(2.68–3.32),17.92 (4.18–5.14)

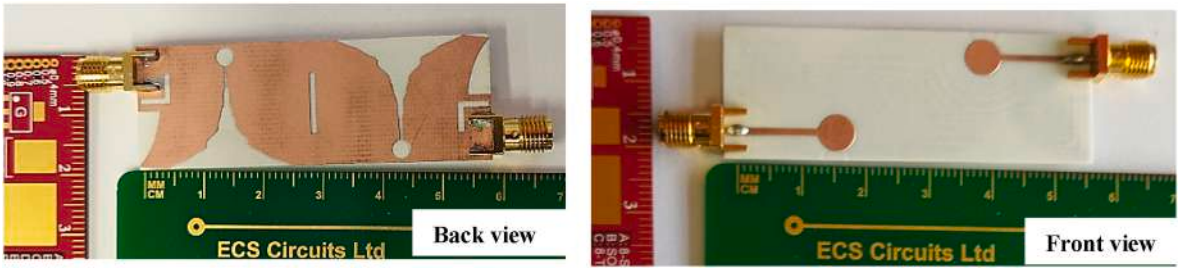

Fig. 6. Compact high isolation UWB two elements VNSMA prototype.

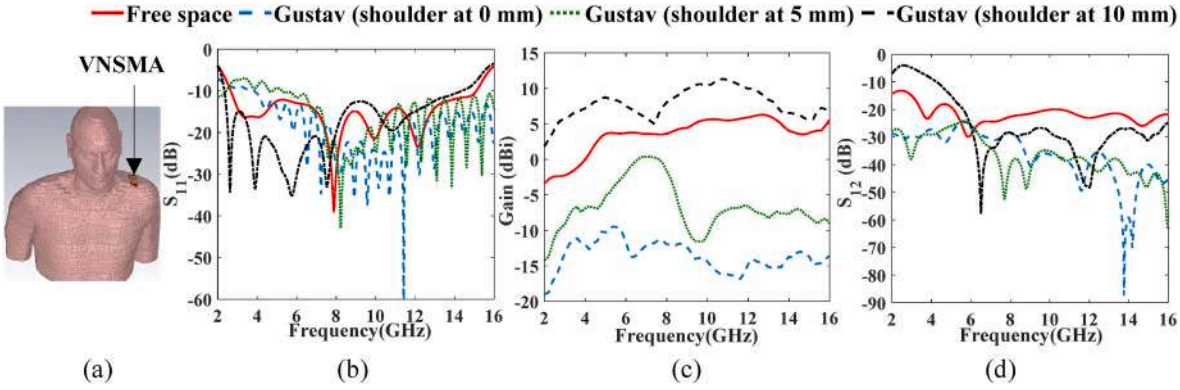

Fig. 7. (a) The proposed UWB VNSMA on the shoulder of CST voxel model, (b) simulated S_{11}, (b) simulated gain, and (d) simulated S_{12}.

optimal. This gap also simulates real-world conditions, providing space for the feeding network [14]. A gab of 10 mm was selected for our work and will be used for SAR calculation. As shown in Fig. 7(b), (c), and 7(d), at the distance of 10 mm and compared to free space, the proposed VNSMA still provides good matching within the required UWB frequency band ($S_{11} < -10.53$ dB at (2.33–14.29 GHz)). Owing to the high dielectric body tissues, the PG is increased by 5.06 dBi, and the isolation at the lower frequency (2.84–3.39 GHz) is reduced to −4.56 dB, as depicted in Fig. 7(b) and (c), respectively. However, a high isolation of −26.67 dB is obtained in the remaining range. It illustrates that the antenna is well-suited for UWB wearable applications.

In addition to the time domain solver, which is based on the Finite Integration Technique (FIT) and offers efficient broadband analysis by capturing the full spectrum of possible interactions, the frequency domain solver, based on the Finite Element Method (FEM), is also employed to provide a more comprehensive and validated analysis, ensuring accurate and reliable on-body and SAR evaluations.

The impact of the body on the proposed antenna, placed at 10 mm

from the shoulder of the CST Gustave voxel model, was analyzed using the FEM method, which is illustrated in Fig. 8, in comparison to the FIT method where in both methods, the required matching and coupling are obtained within the UWB frequency band with increased gain on the voxel model compared to free space.

For safety, the human body should be protected against potentially hazardous electromagnetic radiation by reducing the amount of such electromagnetic exposure from wireless devices, i.e., ensuring SAR is within international limits.

SAR measures the rate at which energy is absorbed by the human body when exposed to an electromagnetic field. It is a critical metric in evaluating the safety of devices that emit electromagnetic radiation, such as mobile phones, wearable antennas, and other wireless communication devices [46]. SAR can be defined as follows:

$$\mathrm{SAR} = \frac{\delta |E|^2}{\rho} \ (\mathrm{W/kg}) \tag{1}$$

where σ is the electrical conductivity of the tissue (S/m), |E| is the root mean square (RMS) value of the electric field strength in the tissue (V/m), and ρ is the mass density of the tissue (kg/m)

Table 5 presents the calculated SAR values for the proposed UWB VNSMA placed 10 mm from the Gustav shoulder, based on CST simulations using the Finite Integration Technique (FIT). These values are calculated for an input power of 100 mW (20 dBm) over 1 g and 10 g masses of actual tissue at various resonance frequencies; results show they don't exceed the safety limits set by the Federal Communications Commission (FCC) and Council of the European Union. Table 6 compares the results obtained in Table 5 using the FIT method with those obtained using the FEM method, demonstrating that both methods achieve acceptably low SAR values.

3. Results in discussion

In this section, the near and far field measurements of the proposed UWB VNSMA are presented, discussed, and compared to the recently published related works. These include reflection coefficient, gain, total efficiency, diversity performance, radiation patterns, and group delay.

Figs. 9–11 show the measured findings for the proposed compact UWB VNSMA. As shown in Fig. 9(a), a sufficiently broad impedance matching of $S_{11} < -11.08$ dB is achieved across the required UWB frequency bands (2.33–14.83 GHz). It shows a 14.8 % BW improvement and 3.72 % size reduction as compared to the single element proposed in Ref. [37] ($S_{11} < -10.89$ dB at 2.9–13.55 GHz). The improved broad impedance matching and reduced size are attributed to edge and tapered slots added to the single element. Using L and vertical slots around the feed line and between the two elements, respectively, enhances their isolation, as illustrated in Fig. 9(b). As illustrated in Fig. 9(b), the MC is less than −18.7 dB at 4.8–5.52 GHz and below −23 dB in most of the operating frequency band, which is suitable for high-performance MIMO systems where isolation of 15–20 dB is typically preferred [47,48]. However, the MC at 2.33–3.12 GHz is below −13 dB, which is generally considered marginal. This affects the antenna's performance in this specific band, leading to negative gain—a common issue in UWB MIMO systems at lower frequency bands, particularly when the antenna size is reduced, as phase cancellation across the antenna becomes more pronounced [49]. Despite the marginal MC at the lower band, the antenna provides low MC across a wide bandwidth of 11.71 GHz (3.12 GHz–14.83 GHz). This is 4.21 GHz more than the typical 7.5 GHz UWB range, ensuring robust performance across most of the frequency spectrum. The phase of the proposed VNSMA is shown in Fig. 9(c).

To test the antenna diversity performance in terms of the independence of the two received signals and the effect of this diversity on the VNSMA radiated power, its Envelope correlation coefficient (ECC) and diversity gain (DG) are calculated and measured as shown in Fig. 9(d) and (e), respectively. The proposed VNSMA provides ECC and DG of 0.002 (Sim. = 0.004) and 9.99 dBi (Sim. = 10 dBi) within the required UWB frequency band as depicted in Fig. 9(d) and (e), respectively, which demonstrates that the proposed UWB VNSMA has good diversity for the practical application, ECC <0.5 and DG≥10 dBi, in terms of low ECC and high DG. According to Ref. [50], the ECC and DG can be defined as follows

$$ECC = \frac{\left|S_{11}^{*}S_{21} + S_{21}^{*}S_{11}\right|^2}{\left(1 - \left(|S_{11}|^2 + |S_{21}|^2\right)\right)\left(1 - \left(|S_{22}|^2 + |S_{12}|^2\right)\right)} \tag{2}$$

$$DG = 10\,x\,\sqrt{1 - |ECC|^2} \tag{3}$$

The measurement setup for far-field results is shown in Fig. 10(a), where port one is terminated with a load of 50 Ω. Fig. 10(b) shows that the measured PG and radiation efficiency provided by the proposed UWB VNSMA is 5.98 dBi (Sim. = 6.27 dBi) and 66–90 % (Sim. = 64–92 %), respectively. The radiation patterns of the proposed UWB VNSMA with stable end-fire and semi omni directional shapes for E-plane and H-plane, respectively, at different frequencies are plotted in Fig. 11. As previously mentioned, the negative gain in the low-frequency bands is due to mutual coupling between the two elements and the reduced size, which causes destructive interference and phase cancellation across the antenna [49], respectively. These results of the proposed VNSAM demonstrate a wide BW, high gain, high DG, low ECC, and stable radiation patterns, making it an excellent option for UWB wearable applications requiring intense penetration and accurate detection, such as microwave imaging (detecting cancers) which we may explore in our

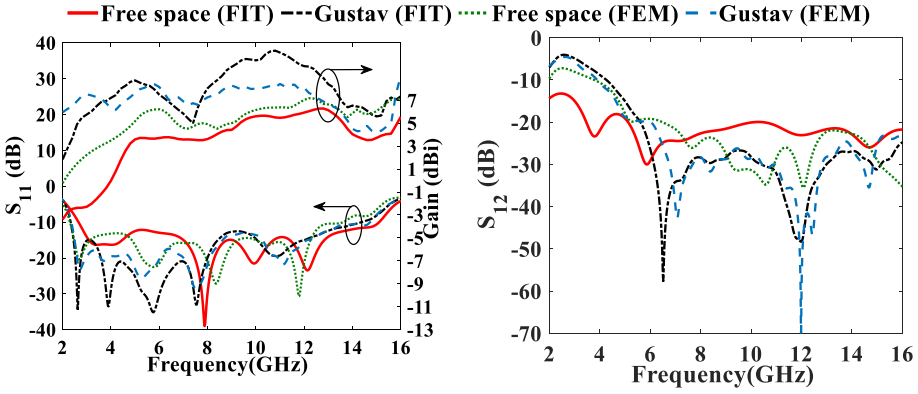

Fig. 8. Difference between the simulated on-body results for the proposed VNSMA using FIT and FEM methods (a) S_{11} with gain (b) S_{12}.

Table 5
SAR calculation for proposed UWB VNSMA on CST voxel model (Gustav) for 100 mW (20 dBm) input power based on FIT method.

Frequency	1 g	10 g
2.64 GHz	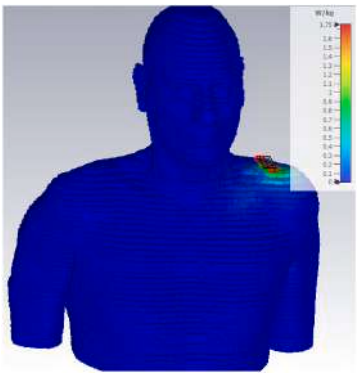	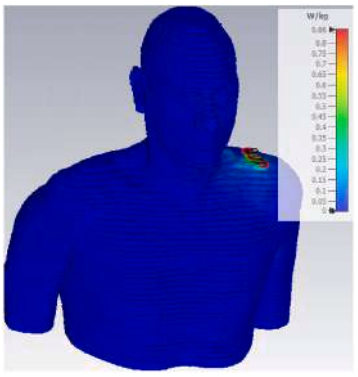
3.91 GHz	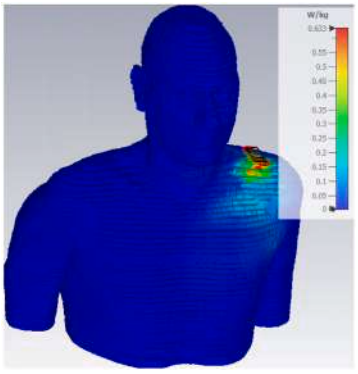	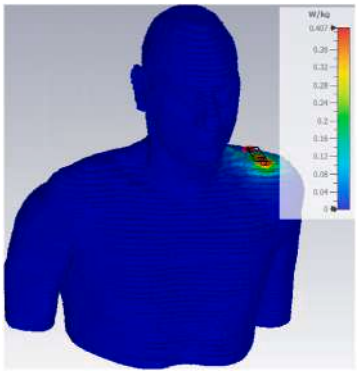
5.74 GHz	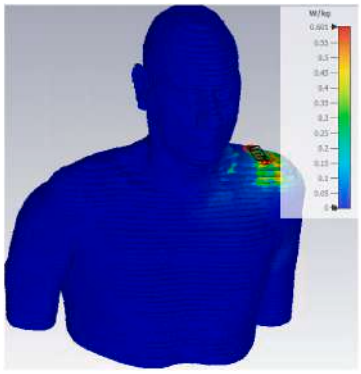	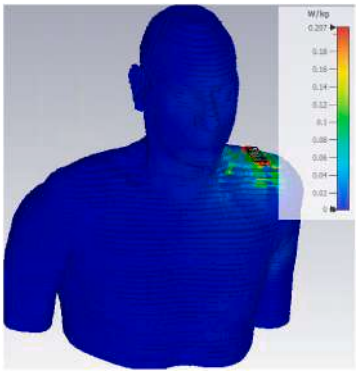
10.88 GHz	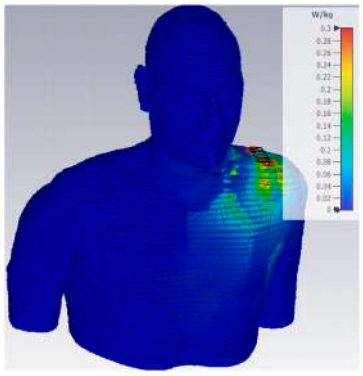	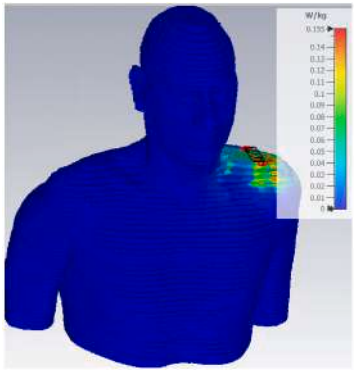

future work. The discrepancy between the simulated and measured is due to the fabrication and measurement tolerances.

It is critical in UWB applications to have an approximate constant group delay (GD) to ensure the capability of handling high-frequency impulses [7]. Fig. 12(a) shows the simulation and measurement setups for obtaining the face-to-face (F2F) GD for the proposed UWB VNSMA. Fig. 12(b) illustrates that the antenna achieves approximately flat-measured GD around 1.2 ns (Sim. = 1 ns) with a variation of less than one ns, which is considered acceptable - almost constant - within the UWB frequency band [7].

Table 6
Comparison of SAR calculations between the FIT and FEM methods of the proposed UWB VNSMA on the CST Gustav voxel model for 100 mW input power.

Method	FIT		FEM	
Frequency	1 g	10 g	1 g	10 g
2.64 GHz	1.75	0.605	1.24	0.44
3.91 GHz	0.86	0.207	0.589	0.166
5.74 GHz	0.633	0.3	0.493	0.244
10.88 GHz	0.407	0.155	0.414	0.177

Table 7 compares the proposed UWB VNSMA with other UWB slot antennas recently published in the literature regarding substrate used (rigid PCB or flexible), antenna type, matching BW, isolation, PG, ECC, DG, MC reduction techniques, and volume. V, GS, SS, and SPG in Table 7 are referred to as Vivaldi, general slot, stepped slot, and slot with protruded ground antennas, respectively. As illustrated in the comparison table, the BW provided by the proposed VNSMA is wider (providing a more extensive data rate) compared to all referenced work, which makes it suitable for UWB high-resolution applications that require precise detection and high accuracy. Compared to the two and four-port MIMO Vivaldi antennas in Refs. [5,36] and the two-port circular ring slot [29],

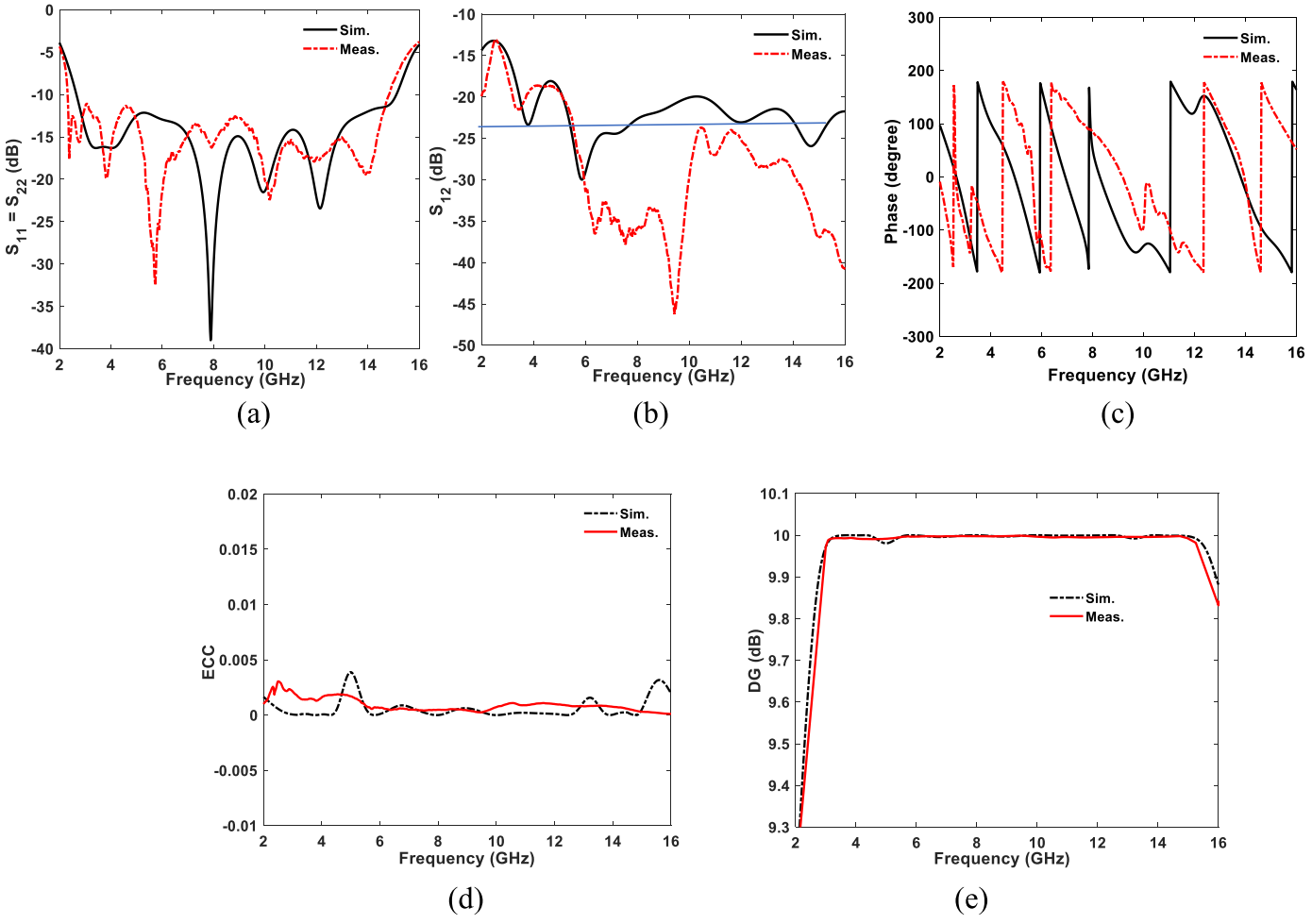

Fig. 9. Simulated and measured (a) S_{11}, (b) S_{21}, (c) phase, (d)ECC, and (e) DG of the proposed UWB VNSMA.

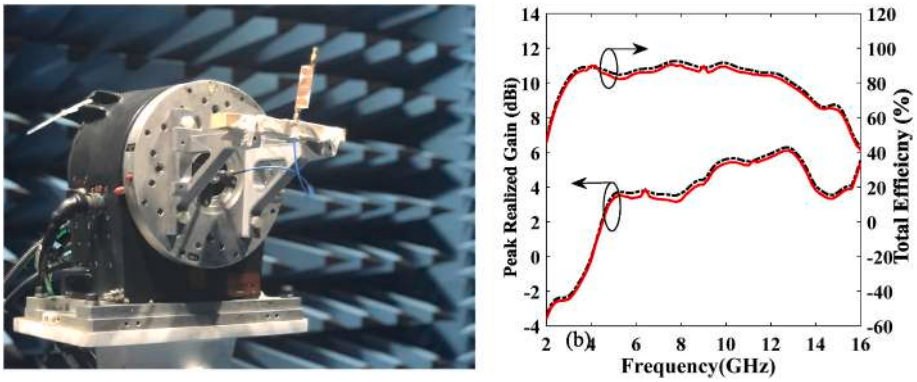

Fig. 10. (a) Measurement setup at the anechoic chamber and (b) simulated and measured realized gain and total efficiency for the proposed UWB VNSMA at port 2.

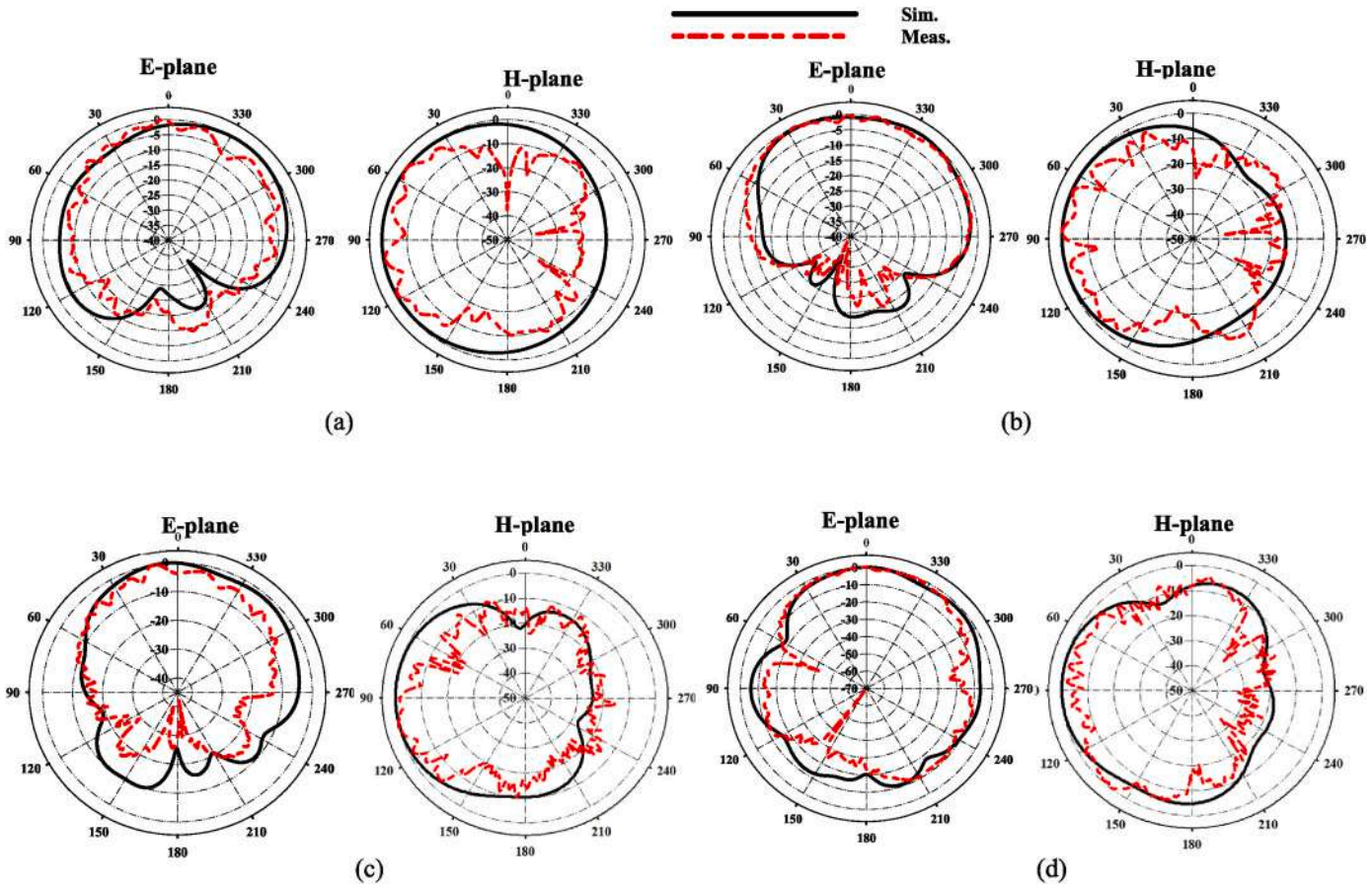

Fig. 11. Simulated and measured radiation patterns of the proposed UWB VNSMA at (a) $f = 5.5$ GHz, (b) $f = 8.5$ GHz, (c) $f = 11.5$ GHz, and (d) $f = 13.5$ GHz.

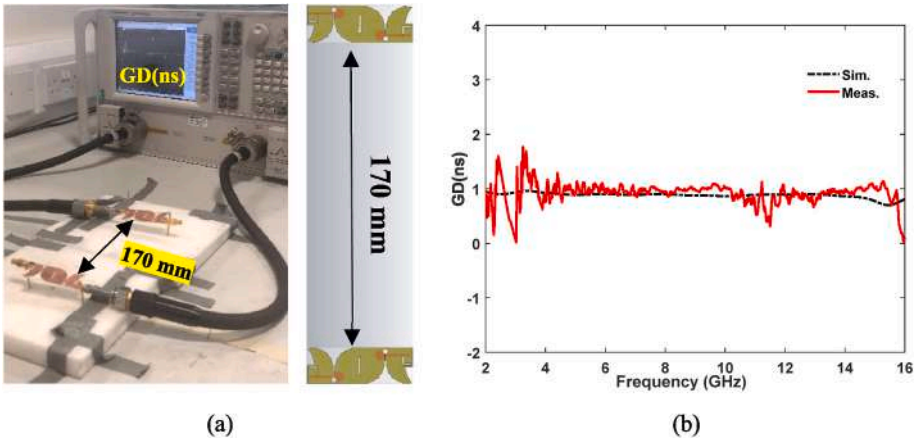

Fig. 12. (a) Measurement and CST setups and (b) Simulated and measured GD of the proposed UWB VNSMA.

the proposed two-port VNSMA provides better matching, wider BW, higher isolation (except at lower bands), lower ECC, and higher DG. Although the size of the proposed VNSMA is 51.1 % and 49.06 % smaller than [5,29], its PG is higher by 12.54 % and 5.18 % (port 2). The PG at port 1 in Ref. [29] and isolation in Ref. [6] are only higher than the proposed VNSMA by 11.4 % and 2 dB despite their 48.9 % and 50.94 % larger size. The size of UWB two-port SS [8,25,28] and SPG [31] MIMO antennas in Table 7 is smaller than the proposed one, and they are the best candidates for mobile communication applications. However, the proposed UWB two-port VNSMA with wider BW, moderate-high gain, and directive radiation patterns are preferred for medical imaging applications that require precise detection of the reflected signals. It may also be employed in WBAN applications to improve communication links that may deteriorate owing to high dielectric losses in human tissues. Our future work will investigate the antenna's performance in these applications.

3.1. *Limitations and future work*

This study provides valuable insights into designing UWB VNSMA for wearable applications, but it is important to acknowledge certain limitations that may have influenced the results. These limitations suggest

Table 7
Comparison with existing UWB MIMO antennas in the literature.

Ref., ports, Type	ε_r	S_{11}(dB), at Freq. Band, BW(GHz)	S_{12}(dB) at Freq. Band,	GD (ns)	PG (dBi)	ECC<, DG> (dB)	MC reduction techniques	Dimensions mm × mm × mm
This work, 2, V	3.55	<-11.08, 2.33–14.83, 12.5	<-23, −13 (2.33–3.12),-18.7 (4.8–5.52)	1.2	3.8–5.98	0.002, 9.99	Tapered edge and vertical slots	57 × 20.26 × 0.813
[5], 2, V	4.4	<-10.5, 3.13–11, 7.87	<-22.55	NA	2.55–5.23	0.06, (Sim: 9.89)	directional properties & slot resonator	60 × 40 × 0.8
[21],2, GS	4.4	2.4–2.485 & 3.1–12.5,9.4	<-25	NA	2–5.5	(Sim:0.01), NA	Orthogonality & ground's edge	56 × 28 × 1
[29], 2, SPG	4.4	<-10, 2.3–12.5,10.2	<-19.5	NA	P1:4–6.75 and P2 G:3.02–5.67	0.01, NA	Fork-shaped stub	48 × 48 × 0.8
[31],2 SPG	4.4	−11.38(P1), −10.21(P2), 2.3–12, 9.7	<-20, −12(2.4), −18.86 (4–4.26)	NA	1.7–4.2	0.04, NA	Orthogonal configuration and λ/4 rectangular slot	32 × 32 × 0.8
[28],2, SS	2.65	<-10,3–11, 8	<-16 (3–3.8), −20	1.25	0.75–3.9(only up to 6 GHz)	0.015, NA	Cross-shaped slot with a metal line	22 × 36 × 0.8
[8],2, SS	4.4	<-11.1, 3.1–10.6,7.5	<-18	NA	2.3–6.73	0.004, NA	T-shaped slot with a narrow slit	22 × 26 × 1.524
[23],4, SS	4.4	<-10 at 3.2–12, 8.8	<-22	NA	−0.82–7.03	0.01, NA	directional radiation & antennas'asymmetricl placements	42 × 25 × 1.6
[25],2, SS	3.5	<-10 dB P1 (3–11.22, 8.2), P2 <-9.32 at 3–11.6, 8.6	<-20.8	NA	-3–1.84	NA, NA	Orthogonality & 45° oriented slot	21 × 30 × 0.762
[6],2, GS	4.3	<-11.92, 2–10.93, 8.93	<-25	NA	3.99 6.27	(Sim:0.004), NA	fence-type decoupling & L-shaped parasitic branches	50 × 35 × 1
[36],4, V	4.4	<-9.8, 3–12.3, 9.3	S_{12} < -15, S_{14} < −20	NA	NA	0.43, 9.65	slots and fence-type structures & I-shape branches	26 × 52 × 0.80

areas for future research, which can build on our findings and further explore in greater depth.

3.1.1. Limitations

The limitations of this work can be summarized as follows.

1. Negative and low gain at lower frequency results due to the compactness that leads to phase cancellation across the antenna [41], where the resulting single element of the proposed UWB VNSMA is 3.72 % smaller than the UWB VNSA. Also, this negative gain at the lower frequency band is attributed to the low isolation at this band, which leads to destructive interference.
2. Low isolation at the lower frequency band is due to the minimal spacing between the VNSA elements (with no space used between them in the proposed UWB VNSMA), leading to destructive interference and causing reduced or even negative gain.
3. The rigid Rogers RO4003C substrate with a thickness of 0.813 mm is not flexible enough for specific wearable applications, where a thinner rigid substrate or a semi-flexible substrate is preferred to withstand mechanical and physical deformation.

3.1.2. Future work

Our future work will focus on To overcome the limitations mentioned above.

1. Investigating techniques to enhance the lower frequency band's low and negative gain, such as adding metamaterials (MTMs) or directors [41]. Details on these techniques can be found in Ref. [39].
2. To reduce high MC between VNSA elements, apply techniques such as incorporating DGS, using electromagnetic bandgap (EBG) structures, implementing neutralization lines, incorporating MTMs, and adding parasitic elements between the antenna elements [49].
3. Semi-flexible substrates such as Rogers RT/duroid 5880 or fabric materials are preferred for wearable applications due to their flexibility, low profile, ease of integration into clothing, and resilience to mechanical changes [39].

4. Conclusions

This paper presents the design, analysis, and fabrication of a new compact two-port Vivaldi Non-uniform Slot MIMO Antenna (VNSMA) for wearable UWB applications. Drawing from Vivaldi non-uniform slot profile antenna (VNSPA) theory, the antenna's design prioritizes wide bandwidth, high gain, and stable radiation patterns crucial for high resolution and precise detection microwave imaging applications such as breast and brain cancer detection. As a novelty in this work, various configurations for placing the two antenna elements were explored to minimize mutual coupling (MC) and optimize performance. Ultimately, positioning the elements side by side at a 180° angle emerged as the most effective configuration. The VNSMA underwent modifications, including etching the ground plane with a vertical slot between the antennas and L-shaped slots around the microstrip-to-slot (M/S) transition to improve port isolation. Additionally, bandwidth and gain improvements were achieved by incorporating exponential tapered and triangular slots at its edges. The proposed VNSMA exhibits a wide 12.5 GHz bandwidth, a moderate gain of 5.98 dBi, high isolation of 18 dB and 23 dB, low ECC of 0.002, high DG of 9.99, and an average group delay of 1.2 ns. The resulting wide BW demonstrates the VNSMA's novelty and ability to cover multiple bands, including WLAN (2.4–2.485 GHz), X-band (8–12 GHz), and part of the Ku band (12–18 GHz).To assess its suitability for wearable applications, the VNSMA is tested on a CST Gustav human phantom, demonstrating promising results with low Specific Absorption Rate (SAR) values across different UWB frequencies. Future research will focus on using various substrate materials to improve compactness, gain, and isolation, especially in the lower frequency band. We will also investigate its performance in microwave imaging applications, such as cancer detection.

CRediT authorship contribution statement

Sahar Saleh: Writing – original draft, Visualization, Validation, Supervision, Software, Resources, Project administration, Methodology, Investigation, Formal analysis, Data curation. **Tale Saeidi:** Writing – review & editing, Supervision, Software, Investigation. **Nick Timmons:** Writing – review & editing, Supervision, Funding acquisition. **Bader Alali:** Visualization, Validation. **Faroq Razzaz:** Writing – review &

editing. **Ayman A. Althuwayb:** Writing – review & editing.

Declaration of competing interest

The authors declare that they have no known competing financial interests or personal relationships that could have appeared to influence the work reported in this paper.

Data availability

Data will be made available on request.

Acknowledgments

This study is supported via funding from Prince Sattam bin Abdulaziz University project number (PSAU/2024/R/1445) and Enterprise Ireland. The authors also want to thank the Center for Wireless Communications (CWI) at Queens University for their assistance with the measurements.

References

[1] S. Saleh, T. Saeidi, N. Timmons, F. Razzaz, A comprehensive review of recent methods for compactness and performance enhancement in 5G and 6G wearable antennas, Alex. Eng. J. 95 (2024) 132–163, https://doi.org/10.1016/J.AEJ.2024.03.097.

[2] M. Kanagasabai, P. Sambandam, M.G.N. Alsath, S. Palaniswamy, A. Ravichandran, C. Girinathan, Miniaturized circularly polarized UWB antenna for body centric communication, IEEE Trans Antennas Propag 70 (2022) 189–196, https://doi.org/10.1109/TAP.2021.3098517.

[3] S. Saleh, T. Saeidi, N. Timmons, Simple compact UWB vivaldi antenna arrays for breast cancer detection, Tele.com (NY) 5 (2024) 312–332, https://doi.org/10.3390/telecom5020016.

[4] P. Kumar, T. Ali, M.P. Manohara, S. Pathan, K. Nayak, T. Khan, A.A. Kishk, A quad port dual band notch UWB MIMO antenna using hybrid decoupling structure, Results in Engineering 23 (2024), https://doi.org/10.1016/j.rineng.2024.102551.

[5] C.-X. Mao, Q.-X. Chu, Y.-T. Wu, Y.-H. Qian, Design and investigation of closely-packed diversity UWB slot-antenna with high isolation, Prog. Electromagn. Res. C 41 (2013) 13–25, https://doi.org/10.2528/PIERC13032301.

[6] L. Wang, Z. Du, H. Yang, R. Ma, Y. Zhao, X. Cui, X. Xi, Compact UWB MIMO antenna with high isolation using fence-type decoupling structure, IEEE Antennas Wirel Propag Lett 18 (2019) 1641–1645, https://doi.org/10.1109/LAWP.2019.2925857.

[7] B.P. Chacko, G. Augustin, T.A. Denidni, Uniplanar slot antenna for ultrawideband polarization-diversity applications, IEEE Antennas Wirel Propag Lett 12 (2013) 88–91, https://doi.org/10.1109/LAWP.2013.2242841.

[8] C.M. Luo, J.S. Hong, L.L. Zhong, Isolation enhancement of a very compact UWB-MIMO slot antenna with two defected ground structures, IEEE Antennas Wirel Propag Lett 14 (2015) 1766–1769, https://doi.org/10.1109/LAWP.2015.2423318.

[9] A. Baz, D. Jansari, S.P. Lavadiya, S.K. Patel, Miniaturized and high gain circularly slotted 4×4 MIMO antenna with diversity performance analysis for 5G/Wi-Fi/WLAN wireless communication applications, Results in Engineering 20 (2023), https://doi.org/10.1016/j.rineng.2023.101505.

[10] C.R. Jetti, V.R. Nandanavanam, Trident-shape strip loaded dual band-notched UWB MIMO antenna for portable device applications, AEU - International Journal of Electronics and Communications 83 (2018) 11–21, https://doi.org/10.1016/j.aeue.2017.08.021.

[11] J.F. Li, Q.X. Chu, Z.H. Li, X.X. Xia, Compact dual band-notched UWB MIMO antenna with high isolation, IEEE Trans Antennas Propag 61 (2013) 4759–4766, https://doi.org/10.1109/TAP.2013.2267653.

[12] Y.Y. Liu, Z.H. Tu, Compact differential band-notched stepped-slot UWB-MIMO antenna with common-mode suppression, IEEE Antennas Wirel Propag Lett 16 (2017) 593–596, https://doi.org/10.1109/LAWP.2016.2592179.

[13] U. Illahi, J. Iqbal, M.I. Sulaiman, M.M. Alam, M.M. Su'Ud, M.H. Jamaluddin, M.N. M. Yasin, Design of new circularly polarized wearable dielectric resonator antenna for off-body communication in WBAN applications, IEEE Access 7 (2019) 150573–150582, https://doi.org/10.1109/ACCESS.2019.2947772.

[14] U. Illahi, J. Iqbal, S.M. Ramay, M.I. Sulaiman, Design and development of a new circularly polarized MIMO wearable DRA for WBAN applications, AEU - International Journal of Electronics and Communications 177 (2024), https://doi.org/10.1016/j.aeue.2024.155208.

[15] M.M. Sani, R. Chowdhury, R.K. Chaudhary, An ultra-wideband rectangular dielectric resonator antenna with MIMO configuration, IEEE Access 8 (2020) 139658–139669, https://doi.org/10.1109/ACCESS.2020.3012793.

[16] M.M. Sani, R. Chowdhury, R.K. Chaudhary, Design and analysis of multiple input multiple output antenna for wideband applications using cylindrical dielectric resonator, AEU - International Journal of Electronics and Communications 131 (2021), https://doi.org/10.1016/j.aeue.2020.153598.

[17] M. Abedian, S.K.A. Rahim, C. Fumeaux, S. Danesh, Y.C. Lo, M.H. Jamaluddin, Compact ultrawideband MIMO dielectric resonator antennas with WLAN band rejection, IET Microw., Antennas Propag. 11 (2017) 1524–1529, https://doi.org/10.1049/iet-map.2016.0299.

[18] S.K. Yadav, A. Kaur, R. Khanna, Compact rack shaped MIMO dielectric resonator antenna with improved axial ratio for UWB applications, Wirel Pers Commun 117 (2021) 591–606, https://doi.org/10.1007/s11277-020-07887-x.

[19] P. Kumari, R.K. Gangwar, R.K. Chaudhary, An aperture-coupled stepped dielectric resonator UWB MIMO antenna with AMC, IEEE Antennas Wirel Propag Lett 21 (2022) 2040–2044, https://doi.org/10.1109/LAWP.2022.3189694.

[20] A.A.R. Saad, H.A. Mohamed, Conceptual design of a compact four-element UWB MIMO slot antenna array, IET Microw., Antennas Propag. 13 (2019) 208–215, https://doi.org/10.1049/iet-map.2018.5163.

[21] S. Mohammad, A. Nezhad, H.R. Hassani, A. Foudazi, A dual-band WLAN/UWB printed wide slot antenna for mimo/diversity applications, Microw. Opt. Technol. Lett. 55 (2013) 461–465, https://doi.org/10.1002/mop.27391.

[22] J. Zhang, L. Wang, W. Zhang, A novel dual band-notched CPW-fed UWB MIMO antenna with mutual coupling reduction characteristics, Progress In Electromagnetics Research Letters 90 (2020) 21–28, https://doi.org/10.2528/PIERL19122703.

[23] G. Srivastava, A. Mohan, Compact MIMO slot antenna for UWB applications, IEEE Antennas Wirel Propag Lett 15 (2016) 1057–1060, https://doi.org/10.1109/LAWP.2015.2491968.

[24] J. Zhu, B. Feng, B. Peng, L. Deng, S. Li, A dual notched band MIMO slot antenna system with Y-shaped defected ground structure for UWB applications, Microw. Opt. Technol. Lett. 58 (2016) 626–630, https://doi.org/10.1002/mop.29632.

[25] S. Koziel, A. Bekasiewicz, Q.S. Cheng, Conceptual design and automated optimisation of a novel compact UWB MIMO slot antenna, IET Microw., Antennas Propag. 11 (2017) 1162–1168, https://doi.org/10.1049/iet-map.2016.0703.

[26] H.T. Chattha, F. Latif, F.A. Tahir, M.U. Khan, X. Yang, Small-sized UWB MIMO antenna with band rejection capability, IEEE Access 7 (2019) 121816–121824, https://doi.org/10.1109/ACCESS.2019.2937322.

[27] P. Debnath, A. Karmakar, A. Saha, S. Huda, UWB MIMO slot antenna with Minkowski fractal shaped isolators for isolation enhancement, Prog. Electromagn. Res. M 75 (2018) 69–78, https://doi.org/10.2528/PIERM18090506.

[28] Y. Zhang, B. Niu, Compact ultrawideband (UWB) slot antenna with wideband and high isolation for MIMO applications, Prog. Electromagn. Res. C 54 (2014) 9–16, https://doi.org/10.2528/PIERC14072304.

[29] P. Gao, S. He, A compact UWB and bluetooth slot antenna for MIMO/diversity applications, ETRI J. 36 (2014) 309–312, https://doi.org/10.4218/etrij.14.0213.0270.

[30] P. Gao, S. He, X. Wei, Z. Xu, N. Wang, Y. Zheng, Compact printed UWB diversity slot antenna with 5.5-GHz band-notched characteristics, IEEE Antennas Wirel Propag Lett 13 (2014) 376–379, https://doi.org/10.1109/LAWP.2014.2305772.

[31] J. Ren, W. Hu, Y. Yin, R. Fan, Compact printed MIMO antenna for UWB applications, IEEE Antennas Wirel Propag Lett 13 (2014) 1517–1520, https://doi.org/10.1109/LAWP.2014.2343454.

[32] D.H. Lidhui, F.S. Zhang, L.X. Cao, Y. Zhao, A compact dual band-rejected MIMO Vivaldi antenna for UWB wireless applications, Progress in Electromagnetics Research Letters 86 (2019) 97–105, https://doi.org/10.2528/pierl19062506.

[33] Z. Li, C. Yin, X. Zhu, Compact UWB MIMO Vivaldi antenna with dual band-notched characteristics, IEEE Access 7 (2019) 38696–38701, https://doi.org/10.1109/ACCESS.2019.2906338.

[34] D.H. Li, F.S. Zhang, G.J. Xie, H. Zhang, Y. Zhao, Design of a miniaturized UWB MIMO Vivaldi antenna with dual band-rejected performance, IEICE Electron. Express 17 (2020) 1–6, https://doi.org/10.1587/ELEX.17.20200233.

[35] A.R.H. Alhawari, T. Saeidi, A.H.M. Almawgani, A.T. Hindi, H. Alghamdi, T. Alsuwian, S.A.B. Awwad, M.A. Imran, Wearable metamaterial dual-polarized high isolation uwb mimo vivaldi antenna for 5g and satellite communications, Micromachines 12 (2021), https://doi.org/10.3390/mi12121559.

[36] J. Nan, H. Zhang, J. Huang, Four-port UWB MIMO vivaldi antenna based on resistor and radiant patch, Prog. Electromagn. Res. M 118 (2023), https://doi.org/10.2528/pierm23033001.

[37] S. Saleh, W. Ismail, I.S.Z. Abidin, M.H. Bataineh, A.S. Al-Zoubi, Novel compact UWB vivaldi non-uniform slot antenna with enhanced bandwidth, IEEE Trans Antennas Propag 70 (2022) 6592–6603, https://doi.org/10.1109/TAP.2022.3161281.

[38] A.M. De Oliveira, A.M. De Oliveira Neto, M.B. Perotoni, N. Nurhayati, H. Baudrand, A. De Carvalho, J.F. Justo, A fern antipodal vivaldi antenna for near-field microwave imaging medical applications, IEEE Trans Antennas Propag 69 (2021) 8816–8829, https://doi.org/10.1109/TAP.2021.3096942.

[39] S. Saleh, W. Ismail, I.S.Z. Abidin, M.H. Jamaluddin, M.H. Bataineh, A.S. Alzoubi, Compact UWB vivaldi tapered slot antenna, Alex. Eng. J. 61 (2022) 4977–4994, https://doi.org/10.1016/j.aej.2021.09.055.

[40] S. Saleh, N. Timmons, J. Morrison, W. Ismail, Compact linearly polarized 5G Vivaldi non-uniform slot filtering antenna, Ain Shams Eng. J. (2023), https://doi.org/10.1016/j.asej.2023.102364.

[41] J. Zhu, B. Feng, B. Peng, L. Deng, S. Li, A dual notched band MIMO slot antenna system with Y-shaped defected ground structure for UWB applications, Microw. Opt. Technol. Lett. 58 (2016) 626–630, https://doi.org/10.1002/mop.29632.

[42] D.M. John, S. Vincent, K. Nayak, S. B S, T. Ali, P. Kumar, S. Pathan, A compact flexible four-element dual-band antenna using a unique defective ground decoupling structure for Sub-6 GHz wearable applications, Results in Engineering 21 (2024), https://doi.org/10.1016/j.rineng.2024.101900.

[43] O. Elalaouy, M. EL Ghzaoui, J. Foshi, A high-isolated wideband two-port MIMO antenna for 5G millimeter-wave applications, Results in Engineering 23 (2024), https://doi.org/10.1016/j.rineng.2024.102466.
[44] H.I. Azeez, H.-C. Yang, W.-S. Chen, Wearable triband E-shaped dipole antenna with low SAR for IoT applications, Electronics (Basel) 8 (2019) 665.
[45] B. Kibret, A.K. Teshome, D.T.H. Lai, Human Body as Antenna and its Effect on Human Body Communications, 2014.
[46] S.M. Ali, C. Sovuthy, S. Noghanian, T. Saeidi, M.F. Majeed, A. Hussain, F. Masood, S.M. Khan, S.A. Shah, Q.H. Abbasi, Design and evaluation of a button sensor antenna for on-body monitoring activity in healthcare applications, Micromachines 13 (2022), https://doi.org/10.3390/mi13030475.
[47] P. Sharma, R.N. Tiwari, P. Singh, P. Kumar, B.K. Kanaujia, MIMO antennas: design approaches, techniques and applications, Sensors 22 (2022), https://doi.org/10.3390/s22207813.
[48] B.T. Ahmed, High isolation compact UWB MIMO antennas, Wirel Pers Commun 128 (2023) 3003–3029, https://doi.org/10.1007/s11277-022-10083-8.
[49] A. Hossain, A.-V. Pham, A novel gain-enhanced miniaturized and lightweight vivaldi antenna, IEEE Trans Antennas Propag (2023) 1–3, https://doi.org/10.1109/tap.2023.3310611.
[50] B. Ali Esmail, S. Koziel, High isolation metamaterial-based dual-band MIMO antenna for 5G millimeter-wave applications, AEU - International Journal of Electronics and Communications 158 (2023) 154470, https://doi.org/10.1016/j.aeue.2022.154470.